



CLICdp-Note-2014-002
14 July 2014

Optimisation Studies for the CLIC Vertex-Detector Geometry

Niloufar Alipour Tehrani^{*†}, Philipp Roloff^{*}

^{} CERN, Switzerland, [†] ETH Zürich, Switzerland*

Abstract

An improved CLIC detector model is under study. This note focuses on the geometry of its vertex detector. Different options fulfilling engineering requirements for the barrel detector and alternative layouts of the endcap regions are considered. The impact of different vertex-detector layouts and of the material budget on the beauty and charm tagging performances for various jet energies and polar angles is being investigated. The study is based on a full detector simulation using GEANT4.

Contents

1. Introduction	4
2. Simulation framework	4
3. Geometries	4
3.1. Coordinate system	5
3.2. The CDR geometry	5
3.3. The <i>spirals</i> geometry	7
3.4. The <i>double_spirals</i> geometry	9
3.5. The <i>double_spirals_v2</i> geometry	13
4. Tracking Performance	14
4.1. The <i>spirals</i> geometry	14
4.2. The <i>double_spirals</i> geometry	15
4.3. The <i>double_spirals_v2</i> geometry	16
5. Flavour-tagging performance	18
5.1. Jet-energy dependence	18
5.2. Jet-angle dependence	19
5.3. Comparison of different layouts	21
5.3.1. <i>spirals</i> and CDR	21
5.3.2. <i>double_spirals</i> and <i>spirals</i>	22
5.3.3. <i>double_spirals</i> and CDR	26
5.4. Impact of the material budget	27
6. Effect of the flavour-tagging performance on the $H\nu\bar{\nu}$ analysis	28
7. Conclusions	29
8. Acknowledgements	30
A. Flavour tagging and jet-angle dependence for the CDR geometry	31
A.1. Jets in dijet events at $\sqrt{s}=1000$ GeV	31
A.2. Jets in dijet events at $\sqrt{s}=500$ GeV	32
A.3. Jets in dijet events at $\sqrt{s}=200$ GeV	33
A.4. Jets in dijet events at $\sqrt{s}=91$ GeV	34
B. Flavour tagging and jet-angle dependence for the <i>spirals</i> geometry	35
B.1. Jets in dijet events at $\sqrt{s}=1000$ GeV	35
B.2. Jets in dijet events at $\sqrt{s}=500$ GeV	36
B.3. Jets in dijet events at $\sqrt{s}=200$ GeV	37
B.4. Jets in dijet events at $\sqrt{s}=91$ GeV	38
C. Flavour tagging and jet-angle dependence for the <i>double_spirals</i> geometry	39
C.1. Jets in dijet events at $\sqrt{s}=1000$ GeV	39
C.2. Jets in dijet events at $\sqrt{s}=500$ GeV	40
C.3. Jets in dijet events at $\sqrt{s}=200$ GeV	41
C.4. Jets in dijet events at $\sqrt{s}=91$ GeV	42

D. <i>spirals</i> vs. CDR	43
D.1. Jets in dijet events at $\sqrt{s}=1000$ GeV	43
D.2. Jets in dijet events at $\sqrt{s}=500$ GeV	44
D.3. Jets in dijet events at $\sqrt{s}=200$ GeV	45
D.4. Jets in dijet events at $\sqrt{s}=91$ GeV	46
E. <i>double_spirals</i> vs. CDR	47
E.1. Jets in dijet events at $\sqrt{s}=1000$ GeV	47
E.2. Jets in dijet events at $\sqrt{s}=500$ GeV	48
E.3. Jets in dijet events at $\sqrt{s}=200$ GeV	49
E.4. Jets in dijet events at $\sqrt{s}=91$ GeV	50
F. <i>double_spirals</i> vs. <i>spirals</i>	51
F.1. Jets in dijet events at $\sqrt{s}=1000$ GeV	51
F.2. Jets in dijet events at $\sqrt{s}=500$ GeV	52
F.3. Jets in dijet events at $\sqrt{s}=200$ GeV	53
F.4. Jets in dijet events at $\sqrt{s}=91$ GeV	54

1. Introduction

The precision physics and experimental conditions at CLIC set challenging requirements on the vertex detector: excellent spatial resolution ($\sim 3 \mu\text{m}$ single-point resolution per layer), time slicing of hits with $\sim 10 \text{ ns}$ precision, geometrical coverage extending down to low polar angles ($\theta_{\min} \approx 8^\circ$), extremely low mass ($\sim 0.2\%X_0$ per detection layer, including readout, support and cabling) and efficient heat removal from sensors and readout. These considerations push the technology beyond the limits of current vertex detectors.

In the CLIC Conceptual Design Report (CDR) [1], simplified vertex detector geometries were used which do not fully take into account the above-mentioned requirements. For example, airflow cooling is considered as a strategy to significantly reduce the amount of material. However, the CDR geometries do not provide a path for the air to flow through the detector. Moreover, the total amount of material per detection layer is optimistically assumed to be $0.1\%X_0$ for the CDR geometries, as detailed models for the cabling and support were not available.

In this study, different options for the vertex barrel and endcap layouts are considered. A spiral arrangement of the sensors in the vertex endcap regions is implemented, allowing for air flow through the vertex-detector volume [2]. Geometries with double-layer arrangements are compared to single-layer layouts. Finally, a geometry with increased material budget is implemented based on engineering studies for supports and cabling.

The study is based on full detector simulations using GEANT4. The performance of each geometry is evaluated by investigating the beauty and charm tagging efficiencies for different jet energies and polar angles. The performances of the implemented geometries are compared [3].

2. Simulation framework

The software chain used to obtain the results shown in this note is the following: the detector geometry is described in a compact XML format which is interpreted by GeomConverter 2.4 [4]. The SLIC v3r0p3 program [5] used to simulate the detector is a thin wrapper around the GEANT4 [6] package. The digitisation and several steps of the event reconstruction are performed using the org.lcsim 2.5 framework [7]. Calorimeter clustering and particle flow analysis are performed by PandoraPFA [8, 9]. Finally, LCFIPlus v00-05-02 [10] is used for flavour tagging. The reconstruction of primary and secondary vertices and the jet finding based on the Durham algorithm [11] are also handled by this package. ILCDIRAC [12] is used to perform the analysis on the computing grid.

In the study presented in this note, beam-induced backgrounds are not included. This choice is made to keep the performance of the vertex-detector geometry separate from the impact of the beam-induced backgrounds. In addition, the required computing time of about 150 CPU years remains at a manageable level.

3. Geometries

The starting point for the studies described in this note is the CLIC_SiD vertex geometry as described in the CDR [1]. This geometry is referred to as the CDR geometry in the following.

Three new geometries are implemented as variations to the CDR layout. The first geometry contains a spiral arrangement of sensors in the vertex endcaps (Section 3.3). The second geometry, in addition to a spiral arrangement of the sensors in the endcap regions, uses double-layered modules for the whole vertex detector (Section 3.4). A third variation with twice the material budget has been used, which takes into account the mechanical support, the readout electronics and the cables (Section 3.5).

3.1. Coordinate system

The right-handed coordinate system in which the detector is described is shown in Figure 1. The beam axis is parallel to the z -axis. The polar angle θ is the angle between the z -axis and the radial coordinate r , and ϕ is the azimuthal angle.

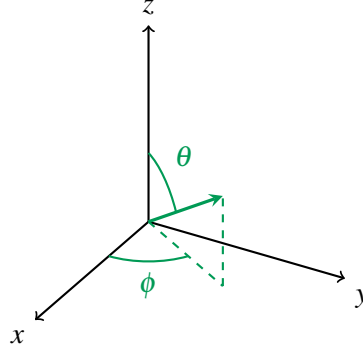


Figure 1: The right-handed coordinate system used to describe the geometry where the beam axis is parallel to the z -axis.

3.2. The CDR geometry

The term "CDR geometry" refers to the CLIC_SiD geometry as defined in [1]. It consists of five concentric layers in the vertex barrel (cf. Figure 2) and four disks in the vertex endcaps.

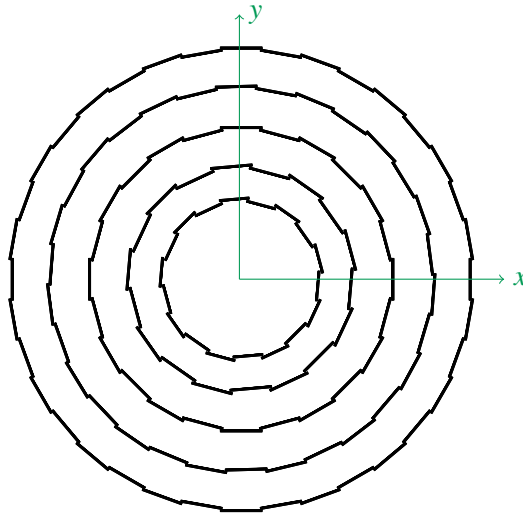


Figure 2: Schematic layout of the vertex barrel detector in the xy -plane for the CDR geometry.

Each layer in the barrel is composed of several modules as listed in Table 1. Each module contains a silicon sensor with a thickness of $50\,\mu\text{m}$. The silicon sensor is the sensitive part of the module which detects the particles passing through it. It is followed by a layer of carbon fiber with a thickness of $130\,\mu\text{m}$, emulating the material for readout, cabling and supports. The total amount of material per layer corresponds to $0.11\%X_0$.

Table 1: Parameters for the vertex detector barrel layers for the CDR geometry. N represents the number of modules in a layer, r the mean radius of the layer, z the half-length and w the width of the module. In the GEANT4 simulations, each module consists of $50\mu\text{m}$ of silicon followed by $130\mu\text{m}$ of carbon fiber. From [13].

Layer	N	$r[\text{mm}]$	$z[\text{mm}]$	$w[\text{mm}]$
1	18	27.0	98.5	9.8
2	18	38.0	98.5	13.8
3	24	51.0	98.5	13.8
4	30	64.0	98.5	13.8
5	36	77.0	98.5	13.8

The vertex detector contains 4 disks in the endcap regions made of silicon pixel detectors with the parameters given in Table 2. Figure 3 shows a schematic layout of the vertex detector with highlighted vertex barrel and endcap. The vertex detector is surrounded by the main tracking system made of silicon strip detectors.

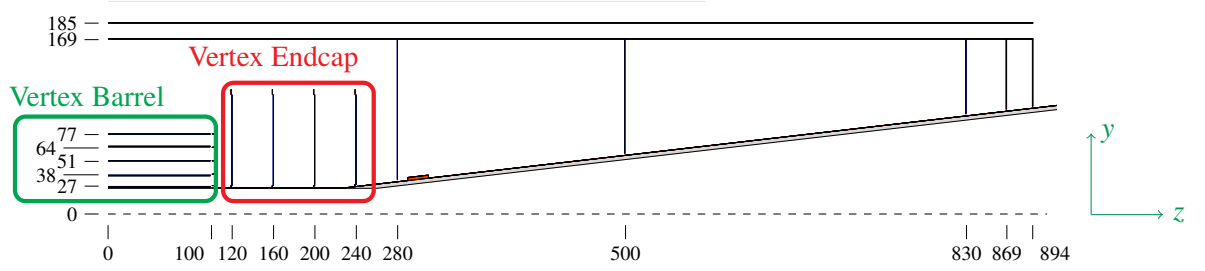


Figure 3: Schematic layout of the vertex detector in the zy -plane. The distances are given in mm. From [13].

Table 2: Parameters for the trapezoidal modules in the forward region of the CDR geometry, where N represents the number of modules in a disk, r_{in} and r_{out} the inner and the outer radius for the disks at the outer edge of the trapezoidal modules, w_{in} and w_{out} the inner and the outer widths and z the position of the modules. In the GEANT4 simulations, each module is made of $50\mu\text{m}$ of silicon followed by $130\mu\text{m}$ of carbon fiber. From [13].

Disk	N	$r_{in}[\text{mm}]$	$r_{out}[\text{mm}]$	$w_{in}[\text{mm}]$	$w_{out}[\text{mm}]$	$z[\text{mm}]$
1	16	27.0	115.0	10.8	45.1	120.0
2	16	27.0	115.0	10.8	45.1	160.0
3	16	27.0	115.0	10.8	45.1	200.0
4	16	28.1	115.0	11.3	45.1	240.0

Figure 4 shows the angular coverage of the vertex barrel and the vertex endcaps separately. The vertex detector can measure tracks down to a polar angle of about $\theta = 8^\circ$. The number of measured points affects the performance of the particle track reconstruction.

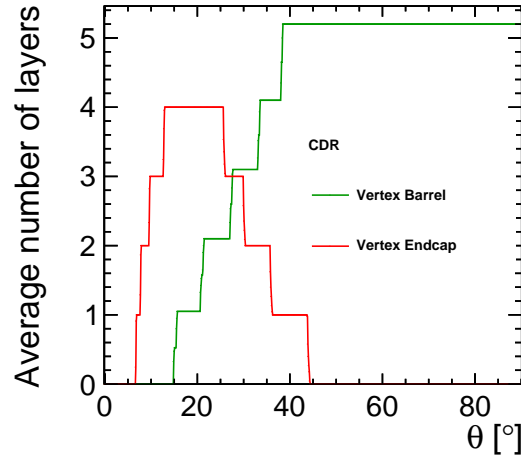


Figure 4: The coverage of the vertex detector with respect to the polar angle θ for the CDR geometry. The number of layers is averaged over the azimuthal angle ϕ .

3.3. The *spirals* geometry

Several engineering studies are in progress to limit the material, e.g. the cables, the mechanical support and also the cooling. Cooling solutions with pipes and liquids increase significantly the material budget. The aim is therefore to use airflow cooling for the CLIC vertex detector.

However, the CDR geometry was not designed for the airflow cooling. The vertex endcaps, which are made of disks, do not allow the air to flow through the vertex detector.

One solution is to use a spiral arrangement for the modules in the endcap regions [2]. Figure 5 illustrates the airflow cooling concept for the vertex detector. The air can flow through the endcap on one side, continue along the barrel sensors and flow out through the other endcap.

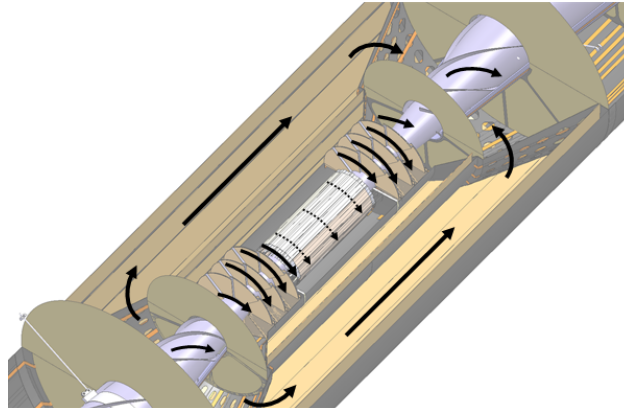


Figure 5: Engineering sketch showing the airflow cooling strategy within the vertex detector. From [2].

The parameters for the spiral arrangement of the sensors in the vertex endcaps are given in Table 3. For this geometry the number of trapezoidal modules N in a layer is reduced to 8 compared to 16 for the CDR geometry. In Table 3, z gives the distance of the first module of each layer to the interaction point in the vertex endcaps and the modules are interspaced by a distance of $\Delta z = 3.6$ mm. The first module in each layer covers the azimuthal angle from $\phi = 157.5^\circ$ to $\phi = 202.5^\circ$.

Figure 6 shows the *spirals* geometry as implemented in the simulations. The barrel geometry is identical to the one of the CDR geometry.

Table 3: Parameters for the trapezoidal modules in the endcap regions of the *spirals* geometry, where N represents the number of modules in a layer, r_{in} and r_{out} the inner and the outer radius at the outer edge of the trapezoidal modules, w_{in} and w_{out} the inner and the outer widths, z the position of the first module of the layer. The other modules are placed at a distance of $\Delta z = 3.6$ mm from the previous module in the z direction. In the GEANT4 simulations, each module is made of $50\text{ }\mu\text{m}$ of silicon followed by $130\text{ }\mu\text{m}$ of carbon fiber.

Layer	N	$r_{in}[\text{mm}]$	$r_{out}[\text{mm}]$	$w_{in}[\text{mm}]$	$w_{out}[\text{mm}]$	$z[\text{mm}]$
1	8	27.0	115.0	22.7	96.6	120.0
2	8	27.0	115.0	22.7	96.6	150.0
3	8	27.0	115.0	22.7	96.6	180.0
4	8	28.1	115.0	23.6	96.6	210.0

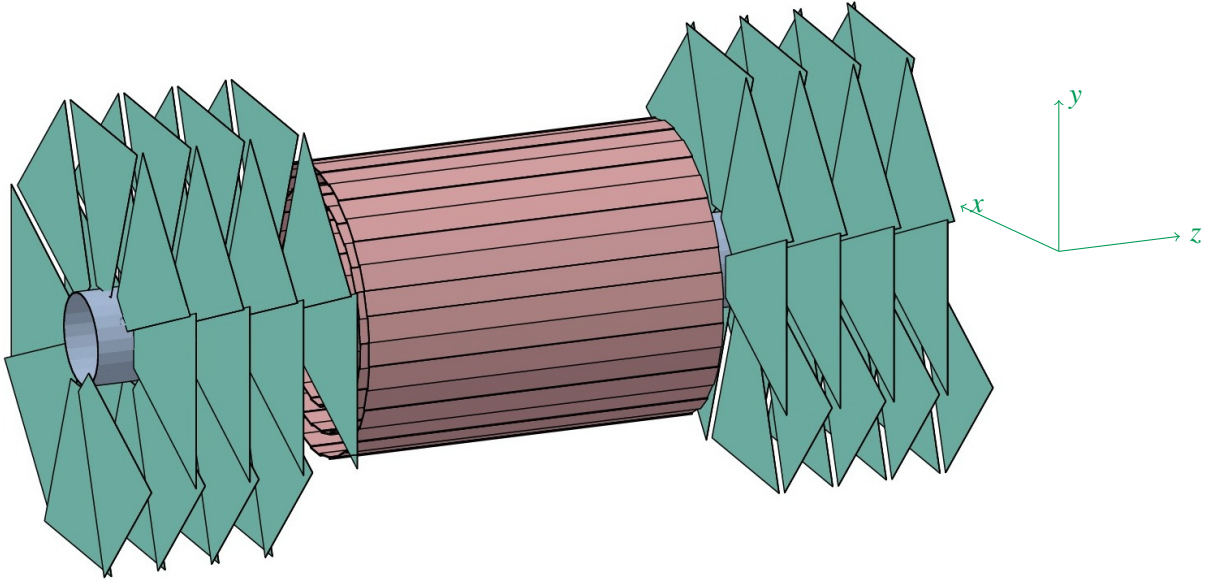


Figure 6: Schematic view of the vertex detector for the *spirals* geometry. The barrel is shown in red and is the same as the CDR barrel. The vertex endcaps modules are shown in green.

To minimise the effect of multiple scattering, a low material budget is required for the vertex detector. Figure 7(a) compares the material budget for the CDR and the *spirals* geometries. For the computation of the material budget we integrate from the interaction point to the outside of the highlighted areas in Figure 3, including the beam pipe and cabling. For each polar angle θ , the material budget is averaged over the azimuthal angle ϕ . As shown in Figure 7(a), the amount of material does not differ much for the *spirals* geometry compared to the CDR layout (the large peak at low polar angles corresponds to the beam pipe).

The number of silicon layers as a function of the polar angles θ averaged over ϕ is given in Figure 7(b) and is very similar for the CDR and the *spirals* geometries. The main difference compared to the disks (see Figure 4) is that the number of layers varies with the ϕ angle.

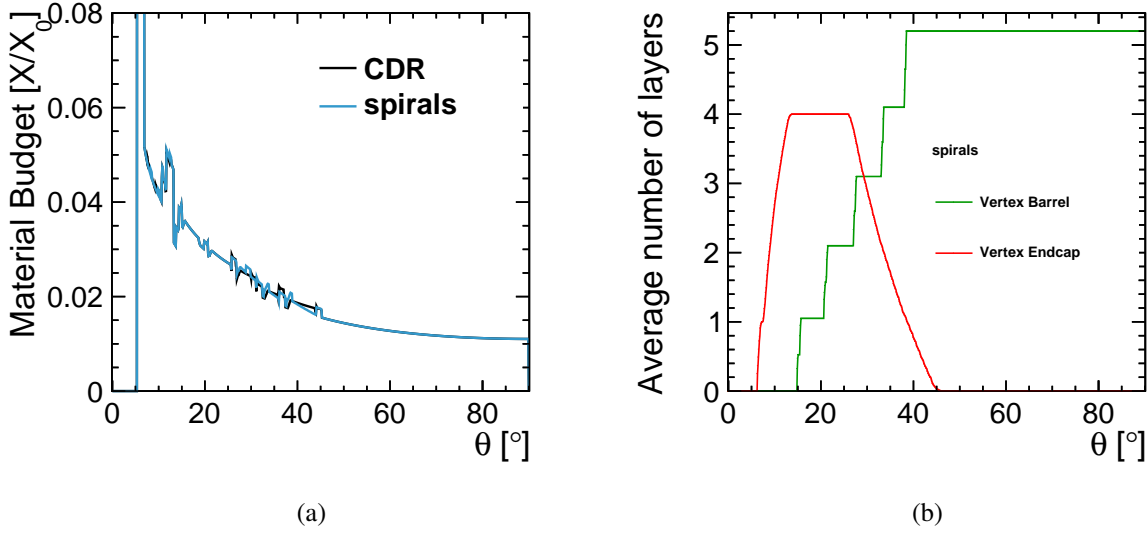


Figure 7: The material budget for the CDR and the *spirals* vertex detectors is shown in (a). The coverage of the vertex detector for the *spirals* geometry with respect to the polar angle θ is shown in (b). The material budget and the number of layers for each polar angle θ are averaged over the azimuthal angle ϕ .

3.4. The *double_spirals* geometry

In the vertex detector, we would like to have as many measurement points as possible and, at the same time, minimise the amount of material. The *double_spirals* geometry uses two silicon sensors on either side of a single mechanical support in the barrel and the endcap regions. As airflow is foreseen for the heat removal of the detector, a spiral arrangement of the modules is used in the endcap regions as in Section 3.3.

In the barrel region, the five layers of single-sided modules are replaced by three layers of double-sided modules. Similarly, in the vertex endcaps, instead of four single layers, there are three double layers in a spiral arrangement.

Both sides of each module contain silicon sensors with a thickness of $50\ \mu\text{m}$ (cf. Figure 8(b)). The overall thickness of the carbon fiber used to emulate the mechanical support, cabling and the electronics is $130\ \mu\text{m}$ (each silicon sensor is followed by $65\ \mu\text{m}$ carbon fiber support) and the rest of the module is filled with air. The overall thickness of a double-layer module is 2 mm and is based on the CLIC_ILD_CDR layout [14] with a material budget of $0.18\%X_0$. A schematic view of the double-layered sensor as implemented in the simulations is shown in Figure 8. The thickness of the carbon per module layer is the same as the one used for the CDR geometry as we assume that the same amount of support structure and cables is used for the single and the double-layered sensors. The parameters of the *double_spirals* geometry are given in Tables 4 and 5. Figure 9 illustrates the vertex detector implemented with double-layered sensors.

Table 4: Parameters of the vertex barrel layers for the *double_spirals* geometry, where N represents the number of modules in a layer, r is the mean radius of the layer, z the half-length of the module and w is the width of the module. Each module is made of two layers of silicon sensors with a thickness of $50\text{ }\mu\text{m}$ plus $65\text{ }\mu\text{m}$ of carbon fiber.

Layer	N	$r[\text{mm}]$	$z[\text{mm}]$	$w[\text{mm}]$
1	18	27.0	98.5	9.8
2	24	51.0	98.5	13.8
3	36	77.0	98.5	13.8

Table 5: Parameters for the trapezoidal modules of the *double_spirals* geometry in the endcap regions, where N represents the number of modules in a layer, r_{in} and r_{out} the inner and the outer radius for the disks at the outer edge of the trapezoidal modules, z the position of the first module of the layer. The other modules are placed at a distance of $\Delta z=5\text{ mm}$ from the previous module in the z direction. For the trapezoidal modules, w_{in} and w_{out} represent the inner and the outer widths. Each module is made of two layers of silicon sensors with a thickness of $50\text{ }\mu\text{m}$ plus $65\text{ }\mu\text{m}$ of carbon fiber.

Layer	N	$r_{in}[\text{mm}]$	$r_{out}[\text{mm}]$	$w_{in}[\text{mm}]$	$w_{out}[\text{mm}]$	$z[\text{mm}]$
1	8	27.0	115.0	22.7	96.6	120.0
2	8	27.0	115.0	22.7	96.6	160.0
3	8	27.0	115.0	22.7	96.6	200.0

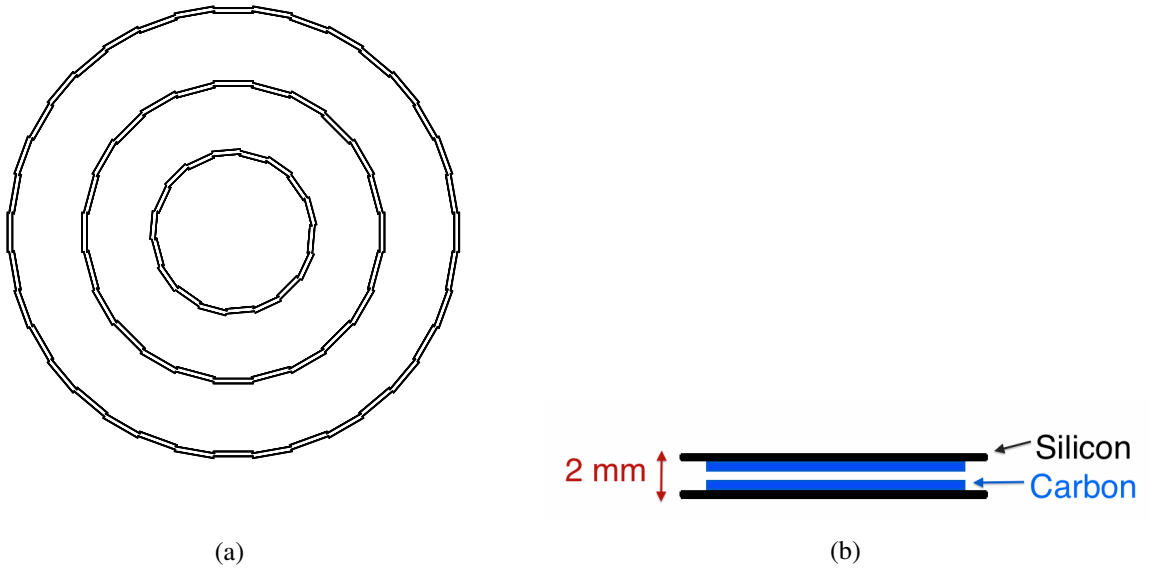


Figure 8: The schematic view of the vertex barrel of the *double_spirals* geometry is shown in (a). In the GEANT4 simulations, each module is implemented as two silicon sensors on top of each other and the overall thickness of the module is 2 mm as illustrated in (b).

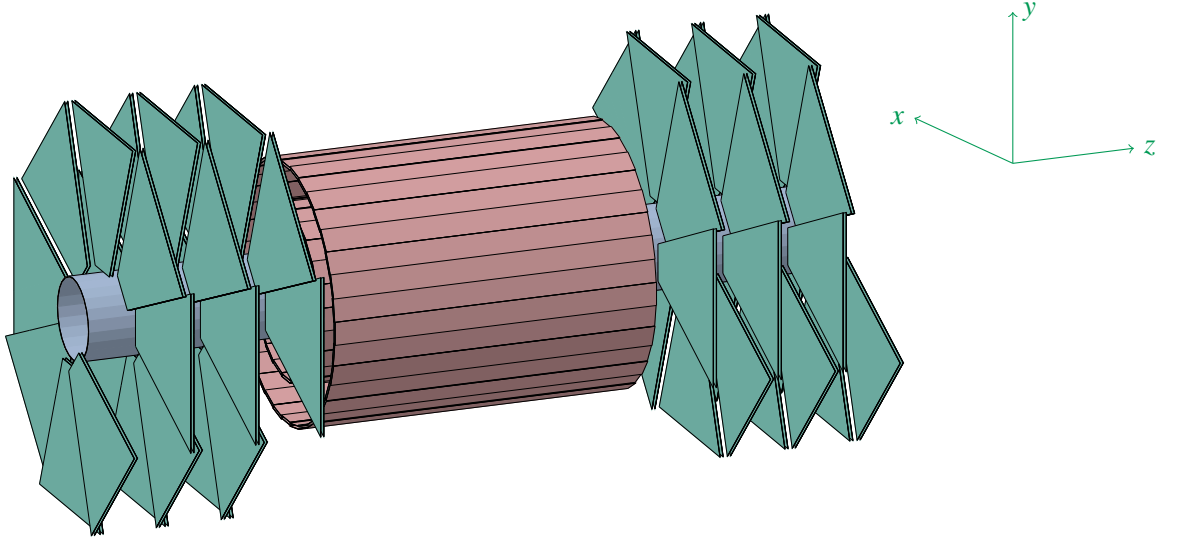


Figure 9: Schematic view of the vertex detector for the *double_spirals* geometry. The barrel region is shown in red and the vertex endcaps in green.

The material budget for the *double_spirals* geometry is shown in Figure 10(a) and is very similar to the CDR geometry. The amount of silicon layers has increased but overall less carbon is needed for the mechanical support.

Figure 10(b) shows the coverage of the *double_spirals* geometry. The average number of layers in the vertex endcaps is higher than for the CDR and the *spirals* geometries with similar material budget (see Figures 4 and 7(b)).

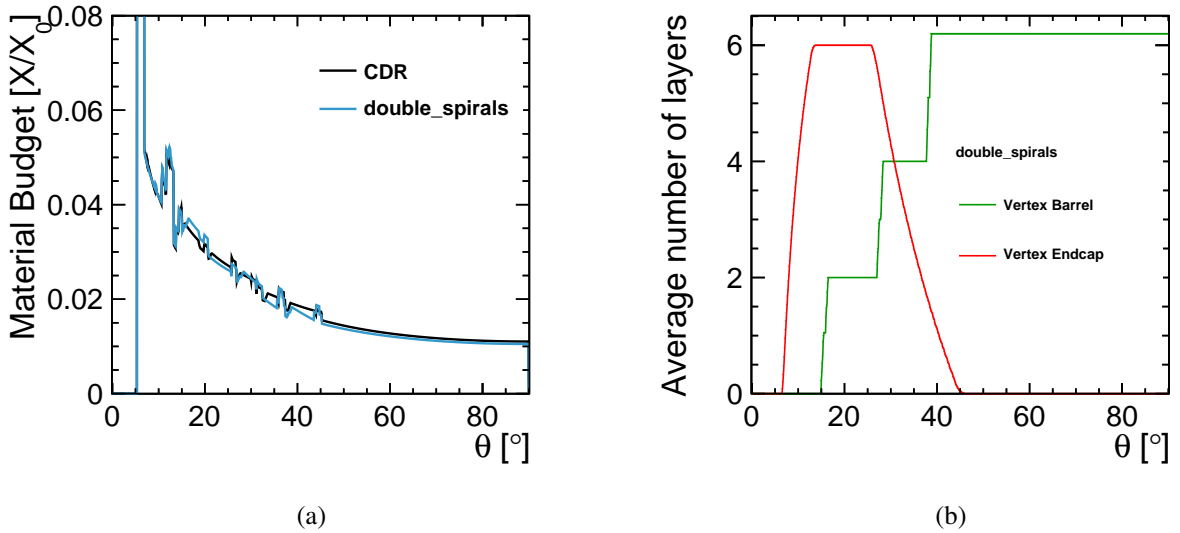


Figure 10: The material budget for the CDR and the *double_spirals* vertex detectors is shown in (a). The coverage of the vertex detector for the *double_spirals* geometry with respect to the polar angle θ is shown in (b). The material budget and the number of layers for each polar angle θ are averaged over the azimuthal angle ϕ .

As a cross-check, we have also calculated the material budget for both geometries at a polar angle of $\theta = 90^\circ$ using the thicknesses of all the material used. The calculated and the simulated values are compared in Table 6. We can observe that both values are quite similar, but the simulation gives higher values. This can be explained by the fact that for the simulation, the material budget is integrated over the ϕ angle and for some azimuthal angles the modules overlap. The calculation, on the other hand, does not consider these overlaps.

Table 6: Calculated and simulated values of the material budget for the CDR and the *double_spirals* vertex barrel at $\theta = 90^\circ$ in units of X_0 .

	CDR	<i>double_spirals</i>
Calculation	1.07%	1.00%
Simulation	1.10%	1.05%

Figure 11 summarizes the coverage of the whole vertex detector (the vertex barrel and endcaps) for the above-mentioned geometries with respect to the polar angle θ (averaged over ϕ). Overall, the *double_spirals* geometry has more sensitive layers in the barrel and the endcaps with similar material budget as the CDR and the *spirals* geometries.

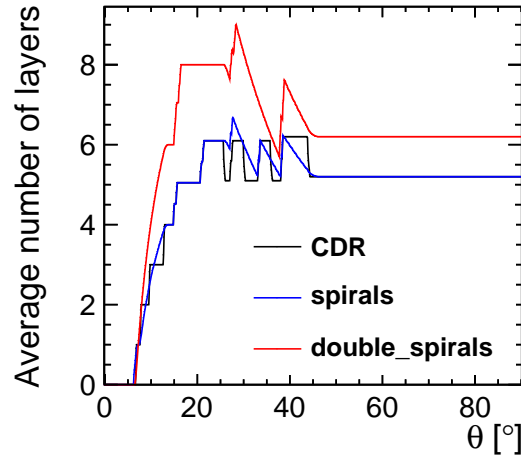


Figure 11: The coverage of the vertex detector for 3 different geometries with respect to the polar angle θ . The number of sensitive layers are averaged over the azimuthal angle ϕ .

Figure 12 shows the number of layers as function of the polar angle θ and the azimuthal angle ϕ for the *spirals* and the *double_spirals* geometries in the endcap regions. For polar angles around $\theta = 40^\circ$, the number of layers becomes very dependent on the azimuthal angle ϕ . In this region, there is a transition between the endcaps and the barrel sections. Using a spiral arrangement of the sensors in the vertex endcaps introduces a ϕ asymmetry in the coverage, see Figures 6 and 9. For some discrete ϕ angles, the number of layers is twice the one at neighbouring ϕ angles (Figure 12). This can be explained by the fact that for a given θ , neighboring modules have a small overlap in ϕ .

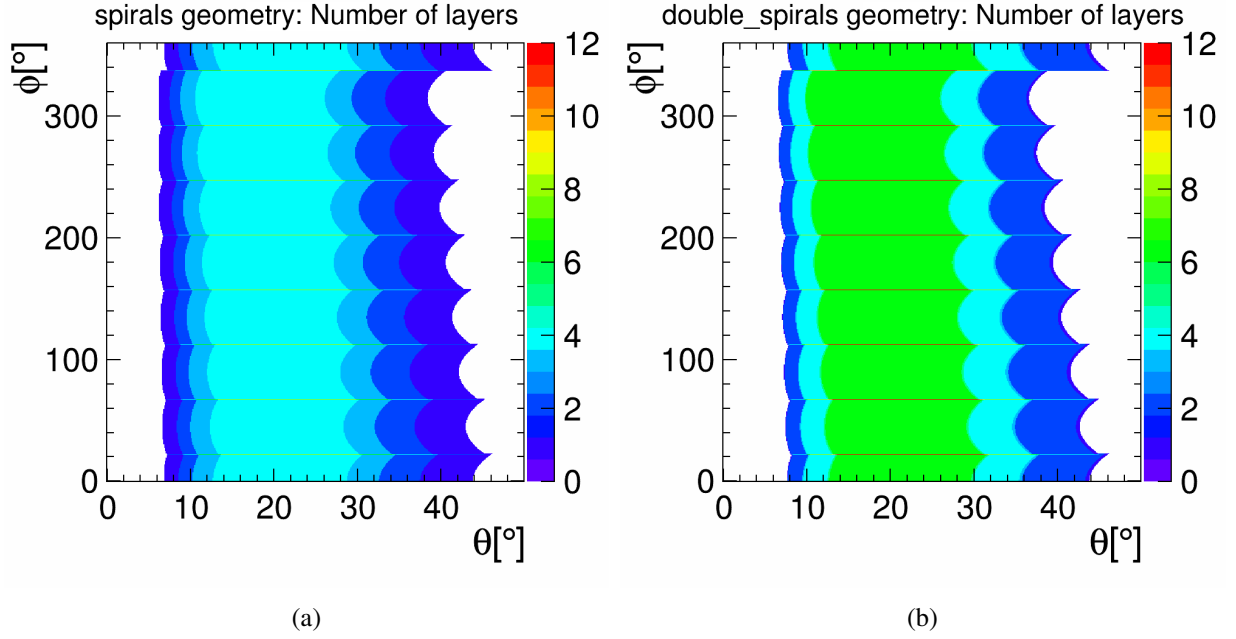


Figure 12: Number of layers as a function of the polar angle θ and of the azimuthal angle ϕ for the *spirals* and the *double_spirals* geometries in the endcap regions.

3.5. The *double_spirals_v2* geometry

In engineering studies, a double-layered module is estimated to have a material budget of $0.4\%X_0$. This value takes into account two silicon sensors with a thickness of $50\mu\text{m}$, the ASIC of $50\mu\text{m}$, the carbon fiber for the mechanical support, the electronics used for the power pulsing and the cables [15].

The *double_spirals_v2* geometry has the same layout as *double_spirals* (cf. Section 3.4), but with a material budget of $0.4\%X_0$ per double layer. In the simulation, this was achieved by modules of silicon followed by $13.5\mu\text{m}$ of copper. The material budget for the *double_spirals_v2* geometry is for example 1.6 times higher at $\theta = 90^\circ$ than that of the CDR geometry as shown in Figure 13.

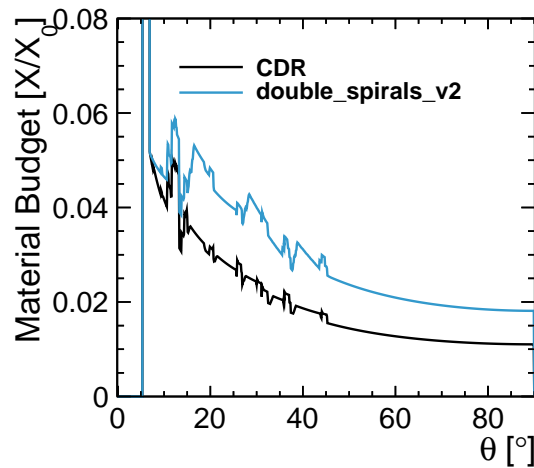


Figure 13: The simulated material budget for the CDR and *double_spirals_v2* geometries. For each polar angle θ , the material budget is averaged over the azimuthal angle ϕ .

4. Tracking Performance

The momentum resolution $\sigma(\Delta p/p^2_{True})$ as well as the transverse $\sigma(\Delta d_0)$ and longitudinal $\sigma(\Delta z_0)$ impact parameter resolutions are compared for the different implemented geometries using single muons with momenta of 1, 10 and 100 GeV for different polar and azimuthal angles. The resolutions are obtained from a Gaussian fit using at least 10000 simulated events and reconstructed tracks. The statistical errors on the impact parameter resolutions are also given in the plots and they are negligible.

4.1. The *spirals* geometry

To study the impact of the *spirals* geometry on the tracking performance, single muons are used with a polar angle of $\theta = 20^\circ$ and azimuthal angles of $\phi = 180^\circ$ or $\phi = 225^\circ$ which hit the first and the last modules of the first endcap layer, respectively. Figure 14 compares the p , d_0 and z_0 resolutions for the CDR and the *spirals* geometries.

The momentum resolutions are very similar in all cases as the measurement of the momentum is dominated by the main tracker. The spiral arrangement affects the d_0 and z_0 resolutions in the forward direction. This can be explained by the fact that the measurement of these two parameters depends on the distance of the vertex layers to the interaction point.

These results are in a reasonable agreement with the results presented in the CDR.

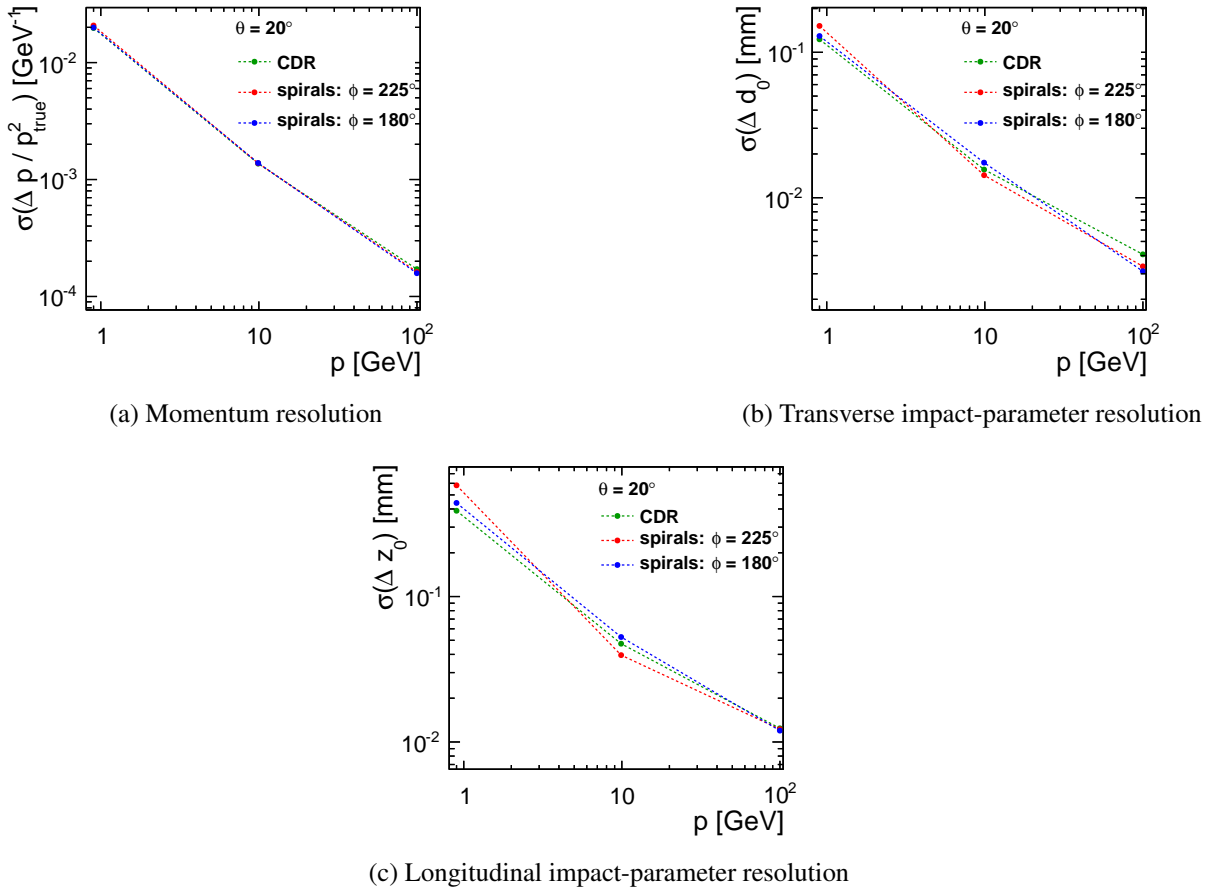


Figure 14: (a) Momentum, (b) transverse impact-parameter and (c) longitudinal impact-parameter resolutions for the CDR and the *spirals* geometries for single muons at $\theta = 20^\circ$.

4.2. The *double_spirals* geometry

The effect of the *double_spirals* geometry on the tracking performance in the barrel region is studied for single muons with a polar angle of $\theta = 90^\circ$ in Figure 15.

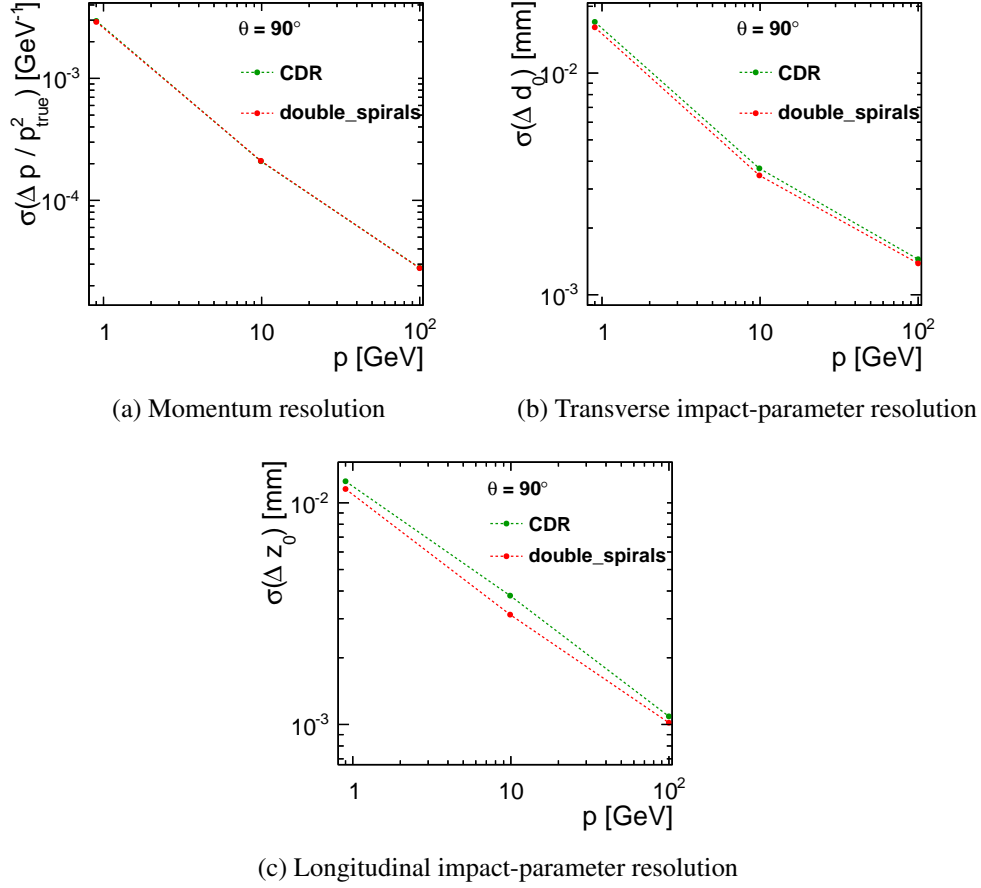


Figure 15: (a) Momentum, (b) transverse impact-parameter and (c) longitudinal impact-parameter resolutions for the CDR and the *double_spirals* geometries for singles muons at $\theta = 90^\circ$.

We can conclude that the use of double-layered modules with 6 sensors in the barrel slightly improves the d_0 and z_0 resolutions, compared to the geometry with 5 single layers (CDR and *spirals* geometries).

4.3. The *double_spirals_v2* geometry

The impact of the *double_spirals_v2* geometry on the tracking performance is studied in the barrel and the endcap regions using single muons with polar angles of $\theta = 90^\circ$ and $\theta = 20^\circ$ in Figures 16 and 17, respectively. For muons at $\theta = 20^\circ$, two different azimuthal angles $\phi = 180^\circ$ and $\phi = 225^\circ$ are considered which correspond to the first and the last module of the first endcap layer. The impact of the material budget on the transverse and longitudinal impact-parameter resolutions is more visible in the barrel region.

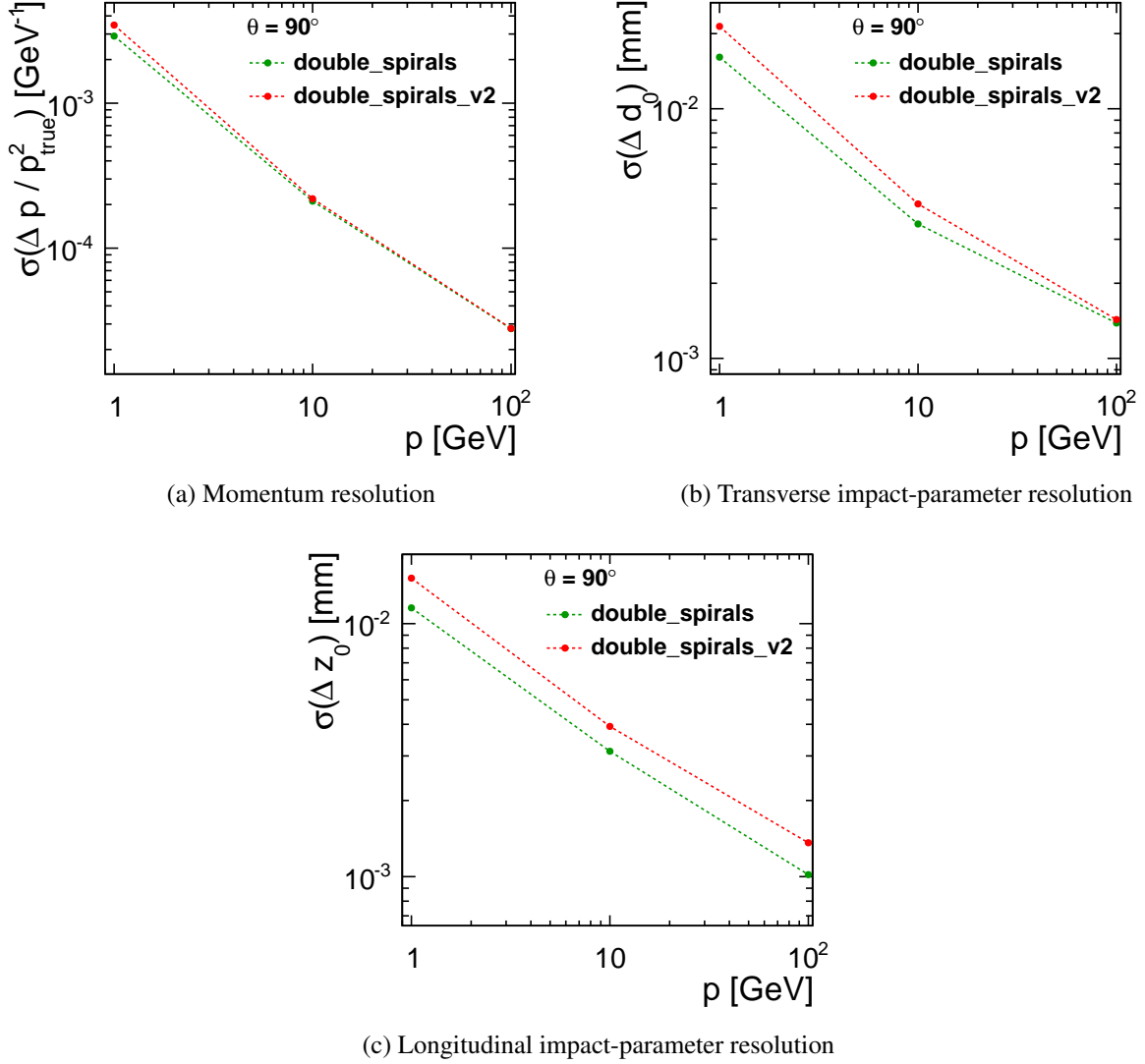


Figure 16: (a) Momentum, (b) transverse impact-parameter and (c) longitudinal impact-parameter resolutions for the *double_spirals* and the *double_spirals_v2* geometries for singles muons at $\theta = 90^\circ$.

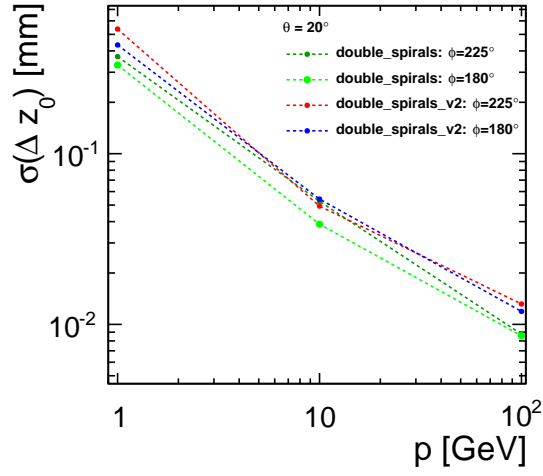
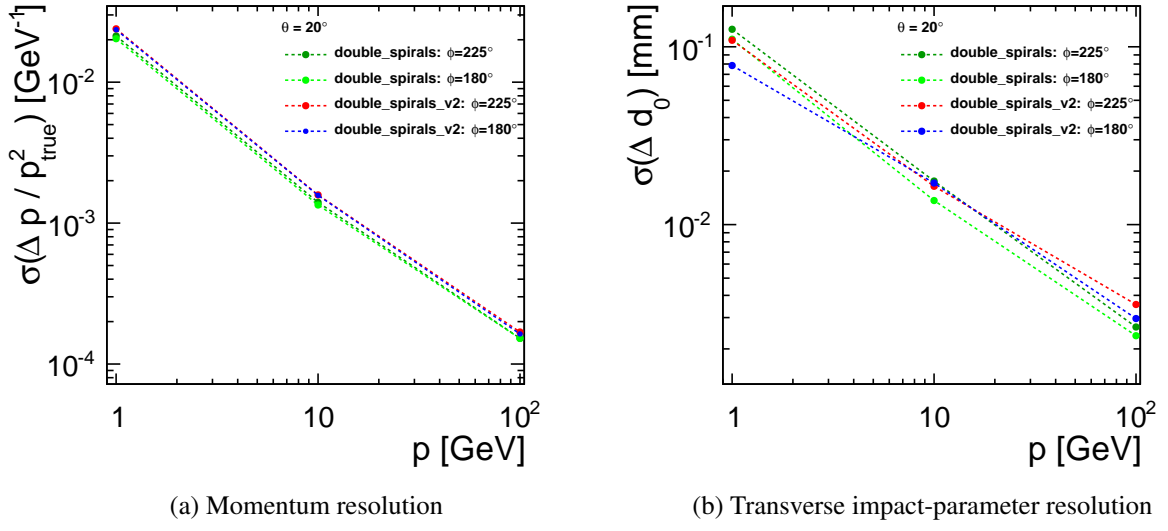


Figure 17: (a) Momentum, (b) transverse impact-parameter and (c) longitudinal impact-parameter resolutions for the *double_spirals* and the *double_spirals_v2* geometries for singles muons at $\theta = 20^\circ$ with azimuthal angles of $\phi = 225^\circ$ or $\phi = 180^\circ$.

5. Flavour-tagging performance

The different geometries described in Section 3 are compared based on their flavour-tagging performance. The flavour tagging is studied using the LCFIPlus package [10].

The performance of the flavour tagging depends on the jet energy and polar angle. For this reason, the study is done considering dijet events with center-of-mass energies, \sqrt{s} , of 91 GeV, 200 GeV, 500 GeV and 1000 GeV having polar angles of $\theta = 10^\circ, 20^\circ, \dots, 90^\circ$ with a uniform distribution in ϕ angles. Initial state radiation (ISR) and beamstrahlung (BS) were switched off during the event generation and hence the final-state quarks are in a back-to-back configuration.

For each jet flavour, energy and angle, 80000 events are used for the following processes:

- $e^+e^- \rightarrow b\bar{b}$
- $e^+e^- \rightarrow c\bar{c}$
- $e^+e^- \rightarrow u\bar{u}$
- $e^+e^- \rightarrow d\bar{d}$
- $e^+e^- \rightarrow s\bar{s}$

The boosted decision trees (BDTs) are trained using 50% of the generated events and the other 50% are used for testing the performance of the flavour tagging.

5.1. Jet-energy dependence

The dependence of the flavour-tagging performance on the jet energy is shown in Figures 18 and 19 using the *spirals* geometry and dijet events at different center-of-mass energies with a mixture of all considered polar angles.

In Figure 18, the fake rate of recognising charm and light flavour (LF) jets as beauty jets is plotted versus the b-tag efficiency. In Figure 19, the fake rate of recognising beauty and light flavour jets as charm jets is plotted versus the c-tag efficiency.

In general, the b-tag performance is better for jets with lower energies. This can be explained by the fact that a B hadron with lower energy has a shorter decay length and therefore decays most likely before the first barrel layer of the vertex detector, while a B hadron with higher energy decays sometimes after the first layer. This leads to a degradation of the track reconstruction and thus the vertex finding and flavour tagging for high-energy jets.

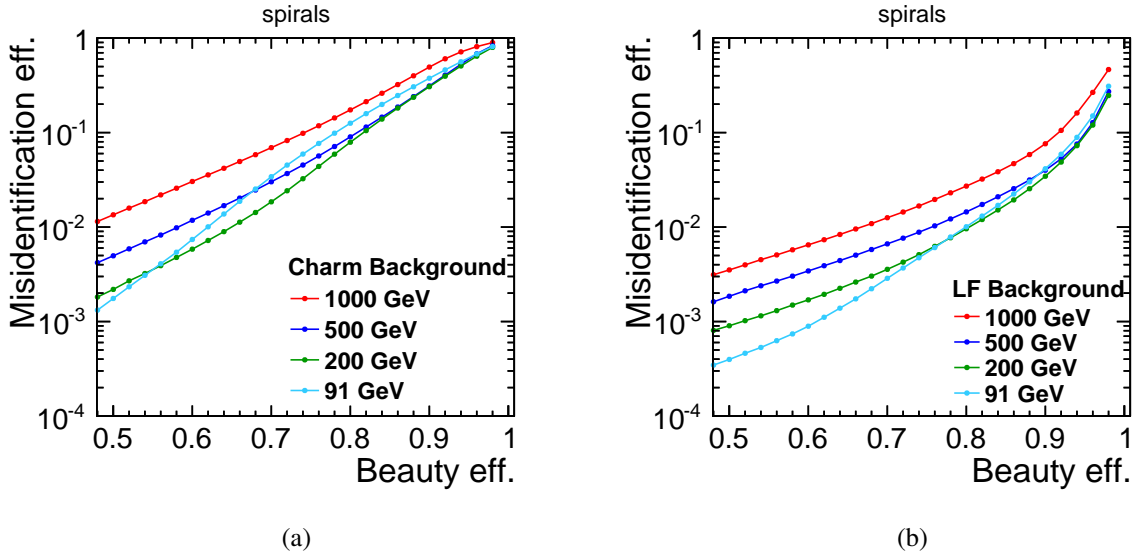


Figure 18: b-tag efficiencies and fake rates for dijets at a mixture of polar angles between 10° and 90° for the *spirals* geometry. (a) shows the fake rate for recognising charm jets as beauty jets and (b) shows the fake rate for recognising light flavour jets as beauty jets.

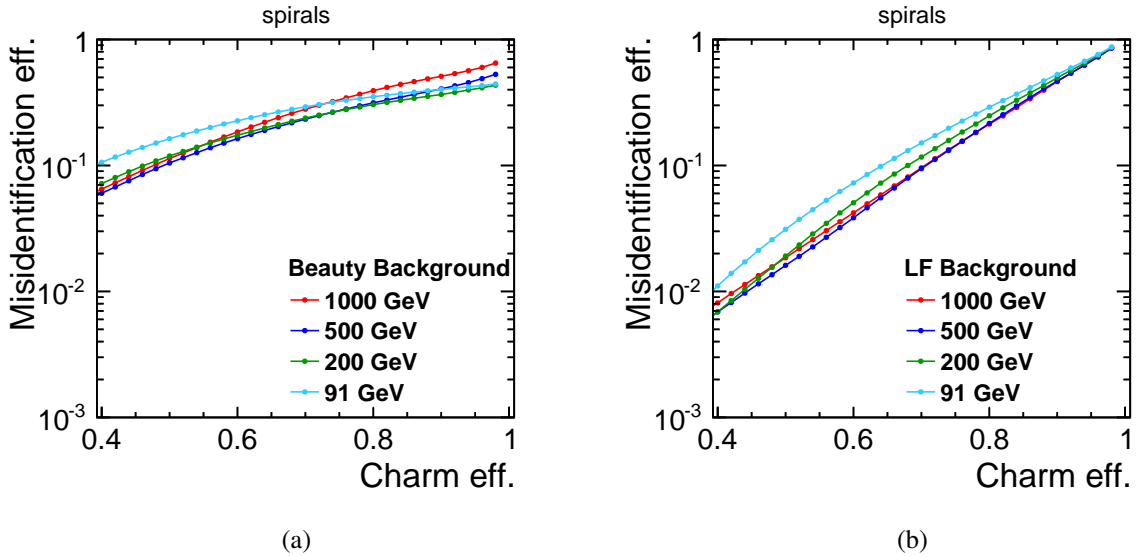


Figure 19: c-tag efficiencies and fake rates for dijets at a mixture of angles between 10° and 90° for the *spirals* geometry. (a) shows the fake rate for recognising beauty jets as charm jets and (b) shows the fake rate for recognising light flavour jets as charm jets.

5.2. Jet-angle dependence

The dependence of the flavour-tagging performance on the jet polar angle is shown in Figures 20 and 21 using the *spirals* geometry for jets in dijet events at $\sqrt{s}=200$ GeV.

In the forward region, several factors are causing the sizeable decrease in performance. For low polar angles, some fraction of particles in the jets is not reconstructed along the beam axis. In addition, the vertex detector resolution in the forward region is worse than in the other parts due to the large distance between the reconstructed vertex and the sensors (cf. Figures 14 and 15). In addition, the number of

sensitive layers decreases with decreasing polar angles (cf. Figure 11).

To illustrate the size of the fluctuations due to the finite size of the event samples used, the statistical uncertainties of the obtained misidentification efficiencies are shown by error bars which are negligible. More results for different jet energies and detector geometries can be found in Appendices A, B and C.

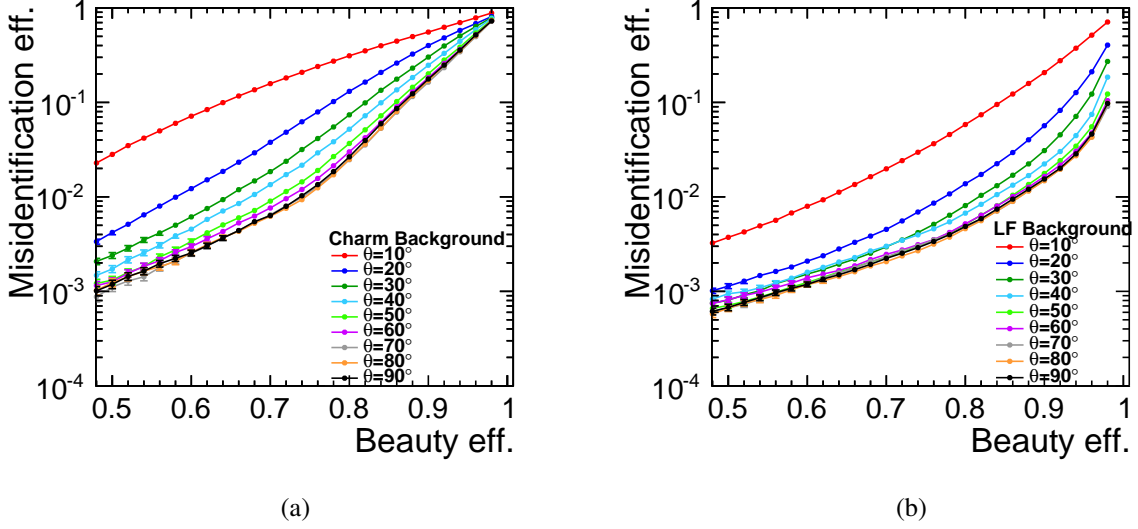


Figure 20: b-tag efficiencies for jets in dijet events at $\sqrt{s} = 200$ GeV with different polar angles using the *spirals* geometry. (a) shows the fake rate for recognising charm jets as beauty jets and (b) shows the fake rate for recognising light flavour jets as beauty jets.

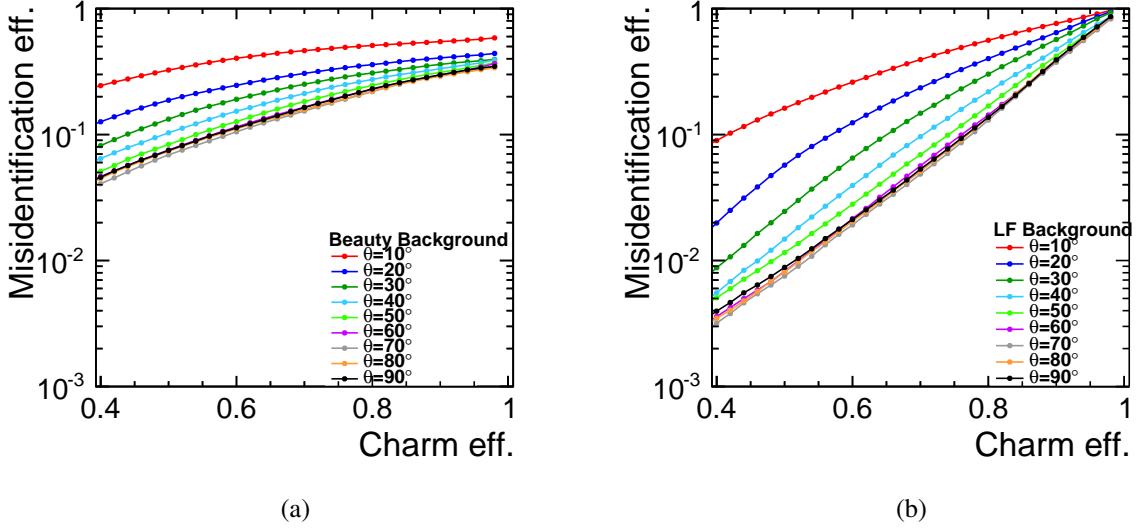


Figure 21: c-tag efficiencies for jets in dijet events at $\sqrt{s} = 200$ GeV with different polar angles using the *spirals* geometry. (a) shows the fake rate for recognising beauty jets as charm jets and (b) shows the fake rate for recognising light flavour jets as charm jets.

5.3. Comparison of different layouts

In the following sections, the different geometries are compared based on their flavour-tagging performance. First, the spiral configuration is compared to the disks in the endcap regions. Then, the double-layered sensors are compared to the single-layered sensors. Finally, the *double_spirals* geometry is compared to the CDR geometry.

5.3.1. *spirals* and CDR

In order to compare two geometries in terms of flavour-tagging performance, the ratio between the misidentification probabilities is computed.

Figures 22 and 23 compare the CDR and the *spirals* geometry using jets in dijet events at $\sqrt{s} = 200$ GeV with polar angles of $\theta = 10^\circ, 20^\circ, 30^\circ$ and 40° . If the ratio between the misidentification probabilities is smaller than one, then the *spirals* geometry has a better flavour-tagging performance than the CDR geometry. Otherwise, the CDR geometry has a better performance. In general, the two geometries have a similar performance. However, the b-tagging performance is up to 20% worse using the *spirals* geometry for jets at $\theta = 40^\circ$. At this angle, there is the transition between the vertex endcaps and the barrel region. With the spiral configuration, the number of sensitive layers becomes dependent on the azimuthal angle ϕ . Less layers can be hit for the spiral configurations in certain ranges in the azimuthal angle ϕ compared to the CDR geometry where the number of layers in the endcap regions does not depend on ϕ (cf. Figure 12). The track-finding algorithm requires a minimum number of layers hit in the vertex detector. This requirement is not dependent on the ϕ direction of the track. Hence with the current software implementation, it is more likely that tracks in a certain ϕ region are missed compared to the CDR geometry. This can be improved in future tracking code with using a ϕ -dependent optimisation of the track finding strategy.

More results for different jet energies can be found in Appendix D.

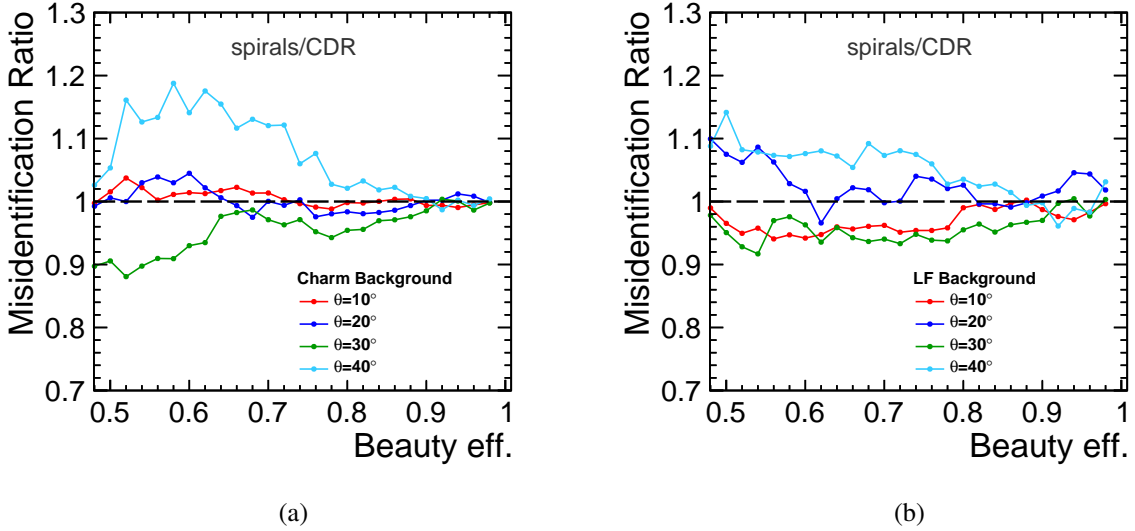


Figure 22: The ratios between the misidentification probabilities for the *spirals* and the CDR geometries as a function of the b-tag efficiency considering the charm (a) and the light flavour (b) backgrounds based on jets in dijet events at $\sqrt{s} = 200$ GeV.

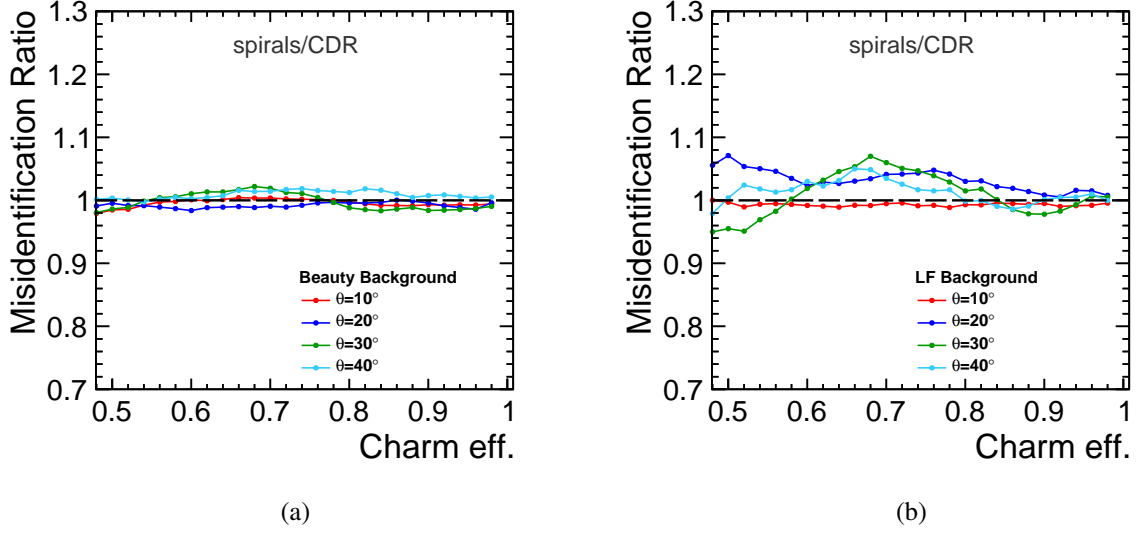


Figure 23: The ratios between the misidentification probabilities for the *spirals* and the CDR geometries as a function of the c-tag efficiency considering the beauty (a) and the light flavour (b) backgrounds based on jets in dijet events at $\sqrt{s} = 200$ GeV.

5.3.2. *double_spirals* and *spirals*

The *double_spirals* and the *spirals* geometries are compared using dijet events with a mixture of polar angles between 10° and 90° . For each jet flavour, 720000 events are included (for each θ value, the same number of events is used). Having large number of events allows to reduce the statistical fluctuations. The comparison between the two geometries is shown in Figures 24, 25, 26 and 27. The performances of these two geometries are similar.

For jets in dijet events at $\sqrt{s} = 1000$ GeV, the *double_spirals* geometry shows a better performance for beauty and charm tagging. For jets in dijet events at $\sqrt{s} = 500$ GeV and $\sqrt{s} = 200$ GeV, the ratio between the misidentification probabilities varies between $\pm 10\%$. For jets in dijet events at $\sqrt{s} = 91$ GeV, the c-tag performance shows better results for light-flavour rejection with the *double_spirals* geometry. This effect might be explained by the fact that double-sided modules provide two measurements which are close to the interaction point and improve the track reconstruction. In some cases, it is possible that the B hadron decays after the first layer in the vertex barrel. In the CDR and the *spirals* geometry, one measurement layer is lost. With the *double_spirals* configuration, two measurement layers are lost. But in total, the number of hits is identical if the decay of the B hadrons occurs after the first layer for the three geometries.

More results for different jet energies and angles can be found in Appendix F.

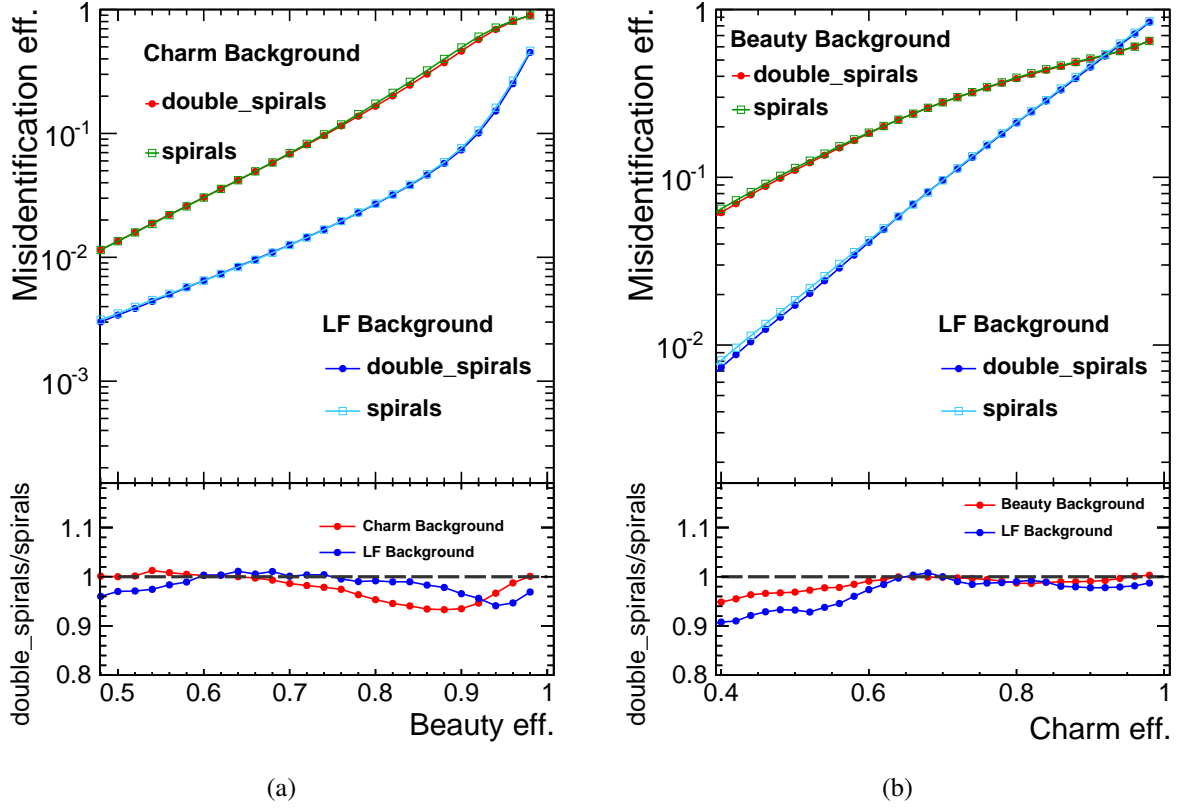


Figure 24: Global comparison between the *double_spirals* and the *spirals* geometries based on beauty tagging (a) and charm tagging (b) for jets in dijet events at $\sqrt{s}=1000$ GeV with a mixture of polar angles between 10° and 90° . On the y-axis, the misidentification probability and the ratio between the misidentification probabilities for the two geometries are given.

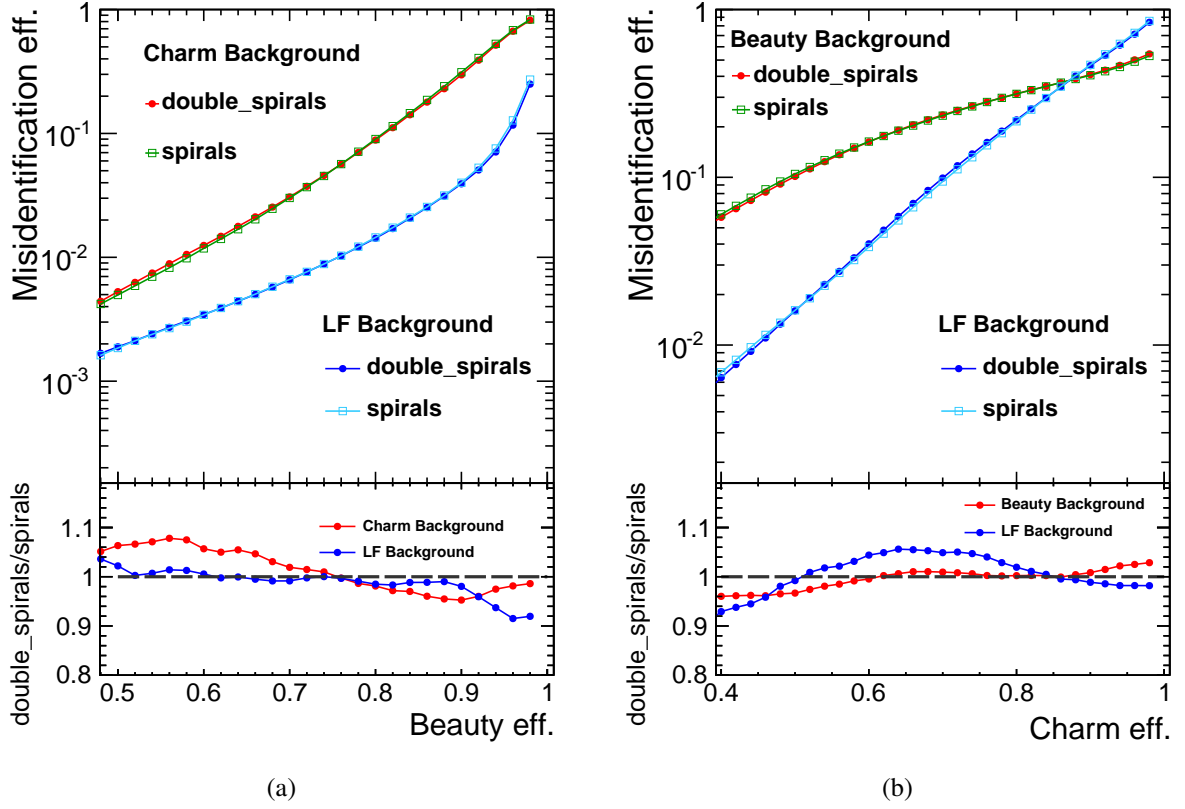


Figure 25: Global comparison between the *double_spirals* and the *spirals* geometries based on beauty tagging (a) and charm tagging (b) for jets in dijet events at $\sqrt{s}=500$ GeV with a mixture of polar angles between 10° and 90° . On the y-axis, the misidentification probability and the ratio between the misidentification probabilities for the two geometries are given.

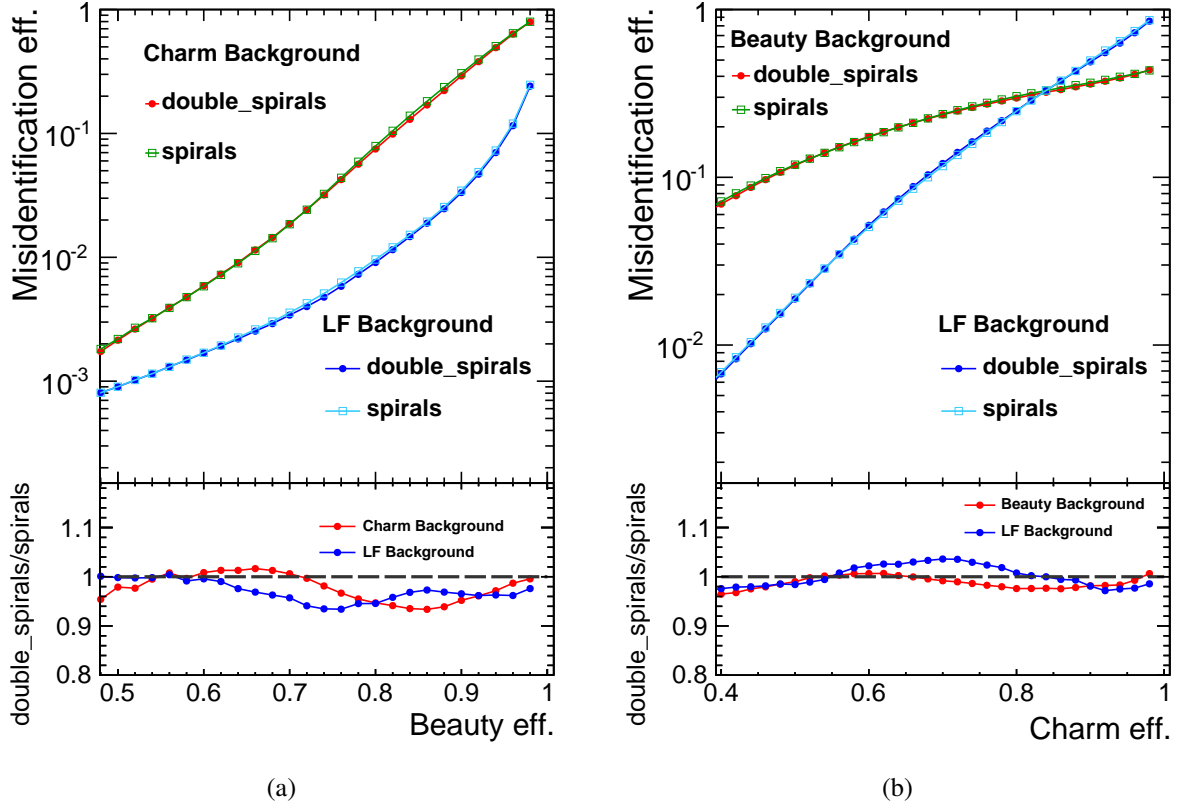


Figure 26: Global comparison between the *double_spirals* and the *spirals* geometries based on beauty tagging (a) and charm tagging (b) for jets in dijet events at $\sqrt{s}=200$ GeV with a mixture of polar angles between 10° and 90° . On the y-axis, the misidentification probability and the ratio between the misidentification probabilities for the two geometries are given.

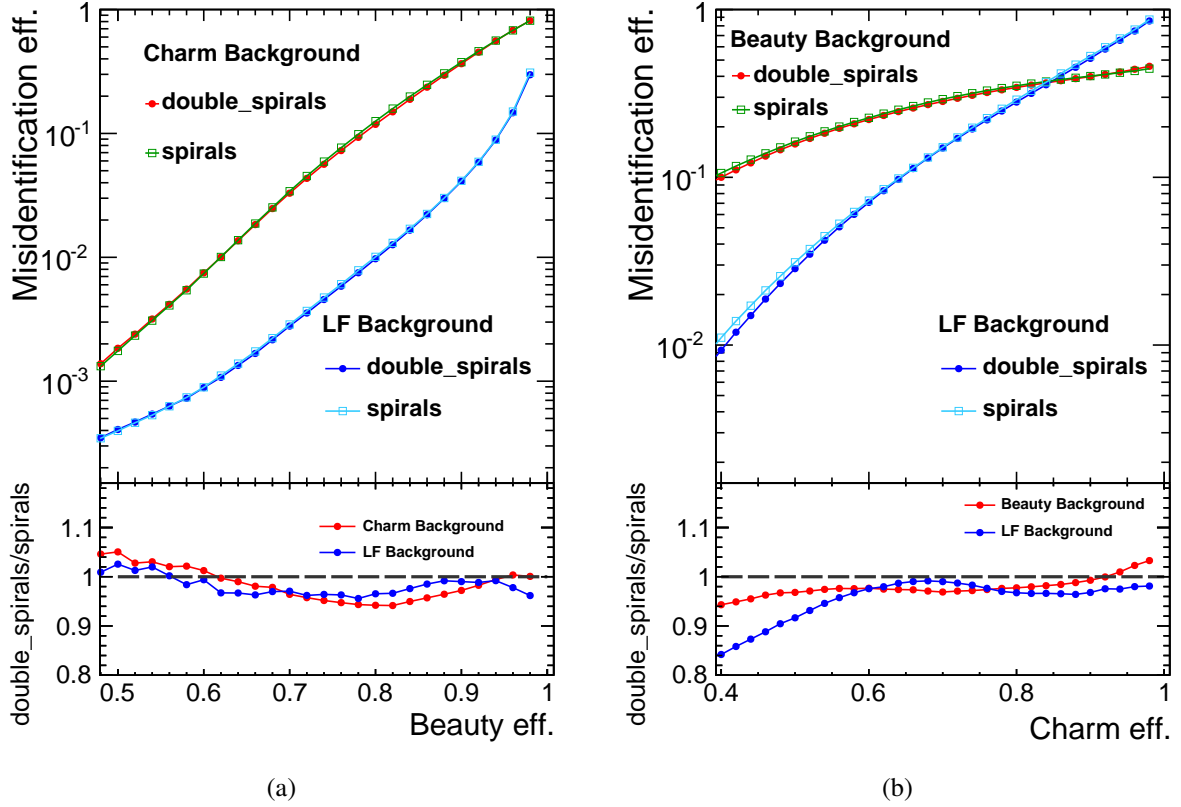


Figure 27: Global comparison between the *double_spirals* and the *spirals* geometries based on beauty tagging (a) and charm tagging (b) for jets in dijet events at $\sqrt{s}=91$ GeV with a mixture of polar angles between 10° and 90° . On the y-axis, the misidentification probability and the ratio between the misidentification probabilities for the two geometries are given.

5.3.3. *double_spirals* and CDR

The comparison between the *double_spirals* and the CDR geometries is given in Figures 28 and 29. In general, the performance of the two geometries is very similar except for dijet events at $\theta = 40^\circ$ where the b-tagging performance for the *double_spirals* geometry decreases by up to 30% (the same effect is also observed when comparing the *spirals* and the CDR geometries in Section 5.3.1). This polar angle falls in the transition region between the vertex endcaps and barrel. The same effect is discussed in Section 5.3.1.

More results for different jet energies can be found in Appendix E.

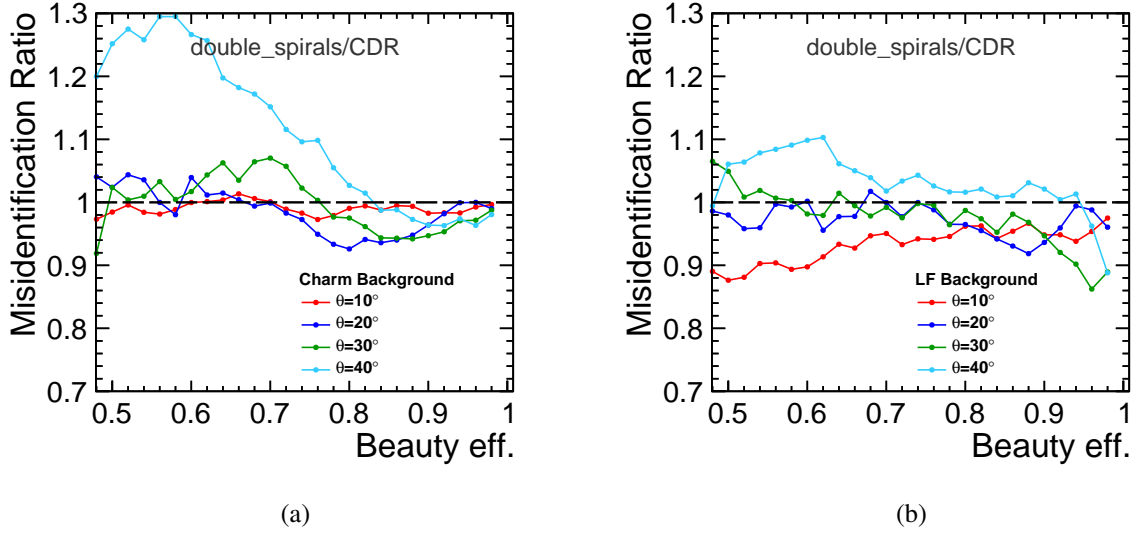


Figure 28: The ratios between the misidentification probabilities for the *double_spirals* and the CDR geometries as function of the b-tag efficiency considering the charm (a) and the light flavour (b) backgrounds based on jets in dijet events at $\sqrt{s} = 200$ GeV.

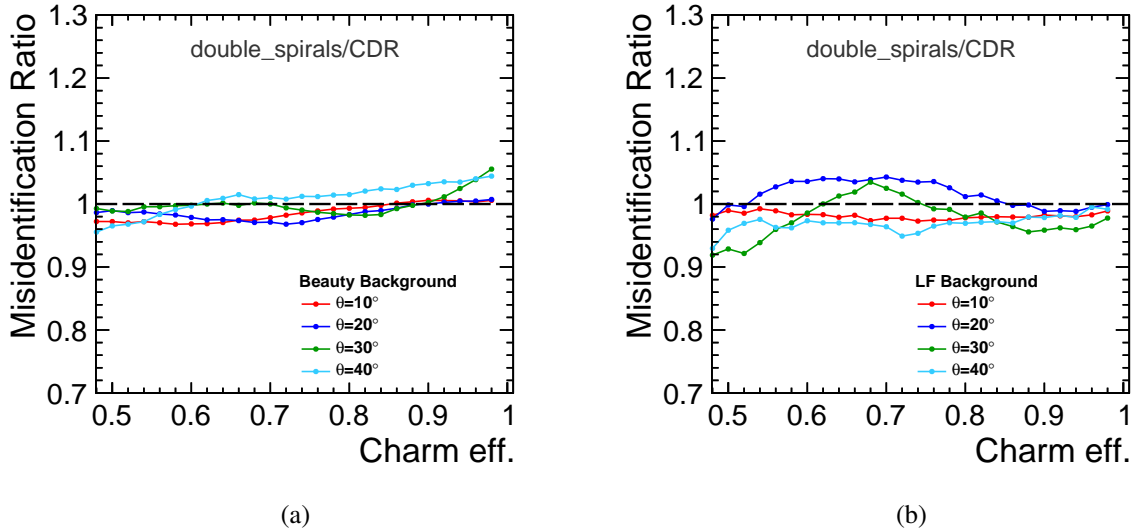


Figure 29: The ratios between the misidentification probabilities for the *double_spirals* and the CDR geometries as function of the c-tag efficiency considering the beauty (a) and the light flavour (b) backgrounds based on jets in dijet events at $\sqrt{s} = 200$ GeV.

5.4. Impact of the material budget

The *double_spirals_v2* geometry is a more realistic version of the *double_spirals* geometry, taking into account the material used for the mechanical support of the sensors and also the material used for the cables. The material budget per double layer is 0.4% X_0 . The flavour-tagging performance of this geometry is given in Figure 30 and compared to the *double_spirals* layout. Dijet events with a mixture of polar angles between 10° and 90° are used for the flavour tagging.

By increasing the material in the vertex detector, the fake rate increases by approximately 5-35% depending on the required signal efficiency and background type.

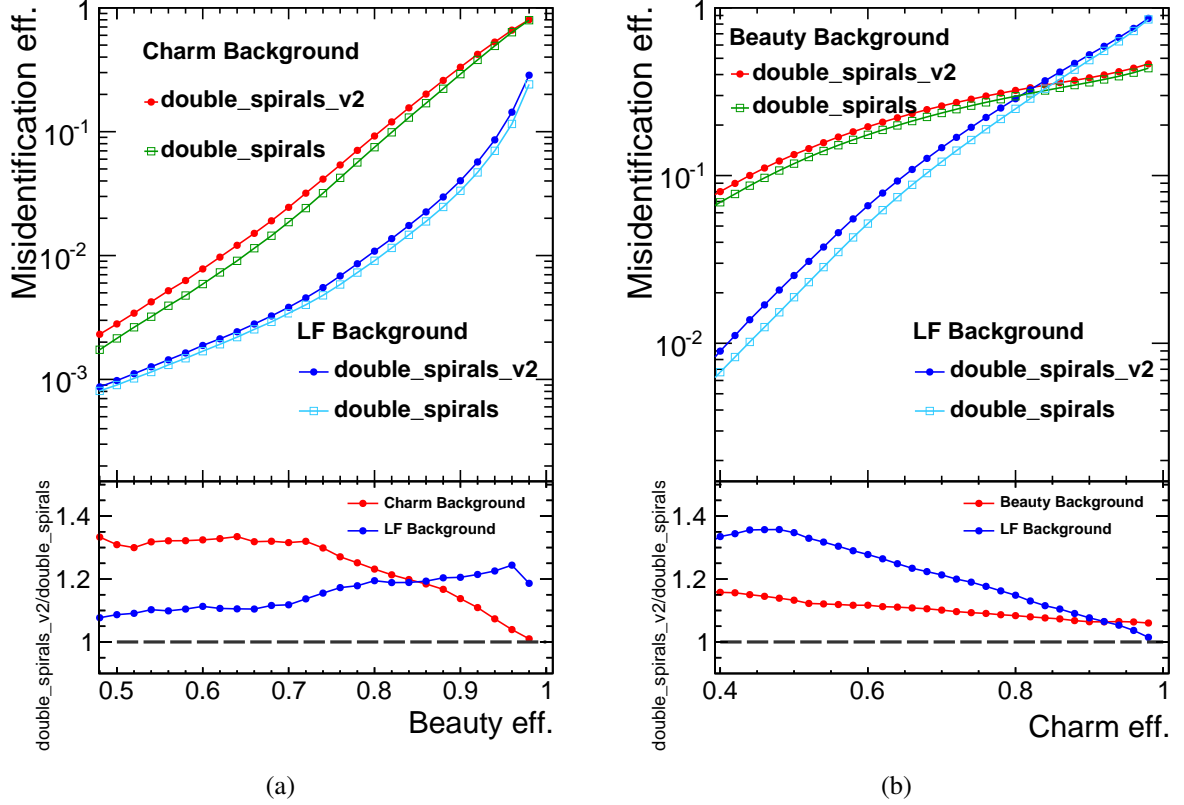


Figure 30: Global comparison between the *double_spirals_v2* and the *double_spirals* geometries based on beauty tagging (a) and charm tagging (b) for jets in dijet events at $\sqrt{s}=200$ GeV with a mixture of polar angles between 10° and 90° . On the y-axis, the misidentification probability and the ratio between the misidentification probabilities for the two geometries are given.

6. Effect of the flavour-tagging performance on the $H\nu\bar{\nu}$ analysis

Flavour tagging is a key ingredient for the measurement of the Higgs boson decay to $b\bar{b}$ and $c\bar{c}$ quark pairs. The Standard Model predicts that the production of the 125 GeV Higgs boson is dominated by the process: $e^+e^- \rightarrow H\nu\bar{\nu}$ at 3 TeV. A study of this process is described in [16] for the CLIC_SiD detector. As shown in the previous sections, changes to the layout and material budget of the vertex detector can lead to changes in the fake rates of typically $\pm 20\%$. We illustrate the effect of this variation of the fake rates on the precision of the $H \rightarrow b\bar{b}$ and $H \rightarrow c\bar{c}$ measurements described in [16].

First, we assume that:

- for $H \rightarrow b\bar{b}$, the backgrounds do not contain b-jets (they are mostly light jets);
- for $H \rightarrow c\bar{c}$, the backgrounds do not contain c-jets (they are mostly beauty and light quark jets);
- the flavour tags are fully uncorrelated with the other selection variables.

Table 7 gives the numbers of events for the decays of the Higgs to $b\bar{b}$ and $c\bar{c}$ quark pairs after the selection performed in the analysis described in [16].

	$H \rightarrow b\bar{b}$	$H \rightarrow c\bar{c}$
Signal events	282×10^3	660×10^1
Background events	130×10^3	350×10^2

Table 7: Number of signal and background events after selection for $H \rightarrow b\bar{b}$ and $H \rightarrow c\bar{c}$ decays. From [16].

If the fake rates increase or decrease by 20%, the number of background events scales by 1.2^2 and 0.8^2 , respectively.

We are interested in the precisions on $\sigma(e^+e^- \rightarrow H\nu\bar{\nu}) \times \text{BR}(H \rightarrow b\bar{b}, H \rightarrow c\bar{c})$, where σ is the cross section and BR the branching ratio. This precision is given by the inverse of the significance which is defined as: $S/\sqrt{S+B}$. S and B are the number of signal and background events, respectively.

Table 8 gives the uncertainties for the default case from [16] and the resulting numbers when the fake rates are increased or decreased by 20%. By comparing the results, the impact of fake rates on $H \rightarrow c\bar{c}$ is higher than $H \rightarrow b\bar{b}$. This can be explained by the fact that the purity for the $H \rightarrow c\bar{c}$ selection is much smaller.

In conclusion, a 20% change in the fake rate for light jets leads to a 6-7% effect on the precision for $H \rightarrow b\bar{b}$. A change of 20% in the light quark and beauty fake rates leads to a 15% change on the precision of $H \rightarrow c\bar{c}$.

Precisions on:	$\sigma(e^+e^- \rightarrow H\nu\bar{\nu}) \times \text{BR}(H \rightarrow b\bar{b})$	$\sigma(e^+e^- \rightarrow H\nu\bar{\nu}) \times \text{BR}(H \rightarrow c\bar{c})$
Default	0.23%	3.1%
20% increased fake rates	0.24%	3.6%
20% decreased fake rates	0.21%	2.6%

Table 8: Uncertainties for the default case (from [16]) and for the cases considering 20% increased and decreased fake rates.

7. Conclusions

A new detector model for CLIC is under development which takes into account the progressing engineering studies while respecting the physics requirements.

Two new layouts for the CLIC vertex detector have been implemented in simulation models: the *spirals* and the *double_spirals* geometries. The spiral arrangement of the modules in the vertex endcaps allows to use airflow cooling which has the potential to reduce the material budget significantly. The *double_spirals* geometry, with the same amount of material budget as the CDR detector, provides more sensitive layers. These two layouts show similar impact parameter resolutions as the CDR geometry.

Flavour tagging is investigated for simulated dijet events using the newly implemented and the CDR geometries. The b-tagging or c-tagging efficiencies versus the fake rates are compared. The overall results show that the implemented geometries are similar in terms of the flavour-tagging performance. We observe that for dijet events with a polar angle θ of around 40° , the flavour tagging degrades for the spiral geometries compared to the CDR geometry. For this polar angle, the number of sensors for the spiral geometries depends on the azimuthal angle ϕ . This effect is worse for double-layered sensors and might be largely compensated using optimisations for the pattern recognition depending on the ϕ -angle. From these results we conclude that the *spirals* and *double_spirals* geometries, a priori, are equally suitable for the vertex detector at CLIC.

The effect of the material budget on the flavour-tagging performance has also been studied. The fake

rates increase by approximately 5-35% when increasing the amount of material per double layer from $0.2\%X_0$ to $0.4\%X_0$.

The effect of the flavour-tagging performance on a physics analysis is illustrated for the process $e^+e^- \rightarrow H\nu\bar{\nu}$ at 3 TeV with subsequent decays $H \rightarrow b\bar{b}$ and $H \rightarrow c\bar{c}$. Changes of the fake rates by $\pm 20\%$ lead to changes in the precisions of the $\sigma \times \text{BR}$ measurements by $\pm 6\text{-}7\%$ for $H \rightarrow b\bar{b}$ and by $\pm 15\%$ for $H \rightarrow c\bar{c}$.

In future extensions of this study, beam-induced backgrounds could be included. This would increase the required computing resources considerably.

8. Acknowledgements

The authors would like to thank Dominik Dannheim, Konrad Elsener and Aharon Levy for their instructive comments on the note. In addition, the authors would like to thank Christian Greife for very helpful discussions on the SiD detector simulation and track reconstruction software.

A. Flavour tagging and jet-angle dependence for the CDR geometry

A.1. Jets in dijet events at $\sqrt{s}=1000$ GeV

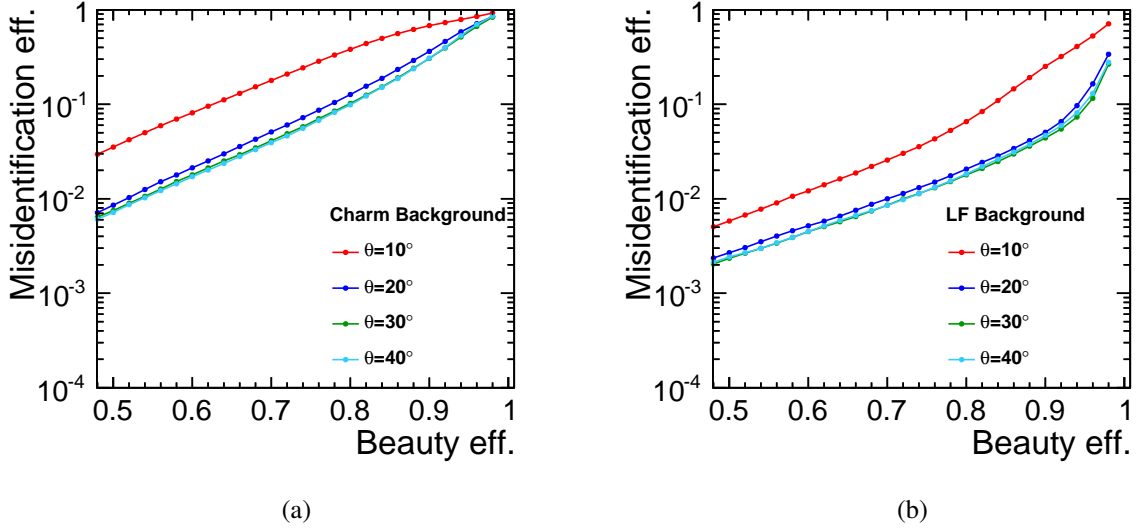


Figure 31: b-tag efficiency for jets dijet events at $\sqrt{s}=1000$ GeV with different polar angles using the CDR geometry.

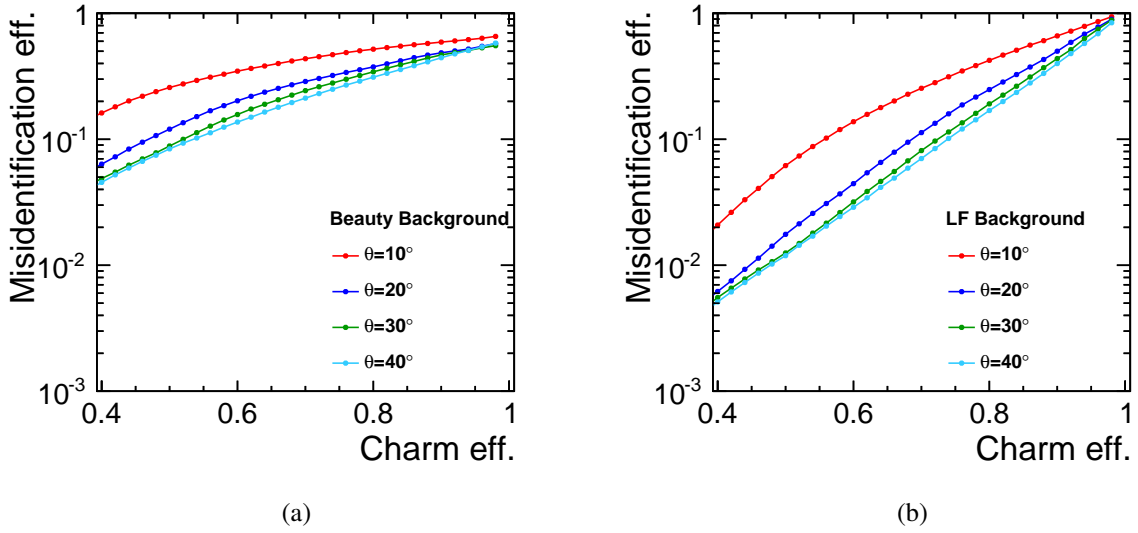


Figure 32: c-tag efficiency for jets in dijet events at $\sqrt{s}=1000$ GeV with different polar angles using the CDR geometry.

A.2. Jets in dijet events at $\sqrt{s}=500$ GeV

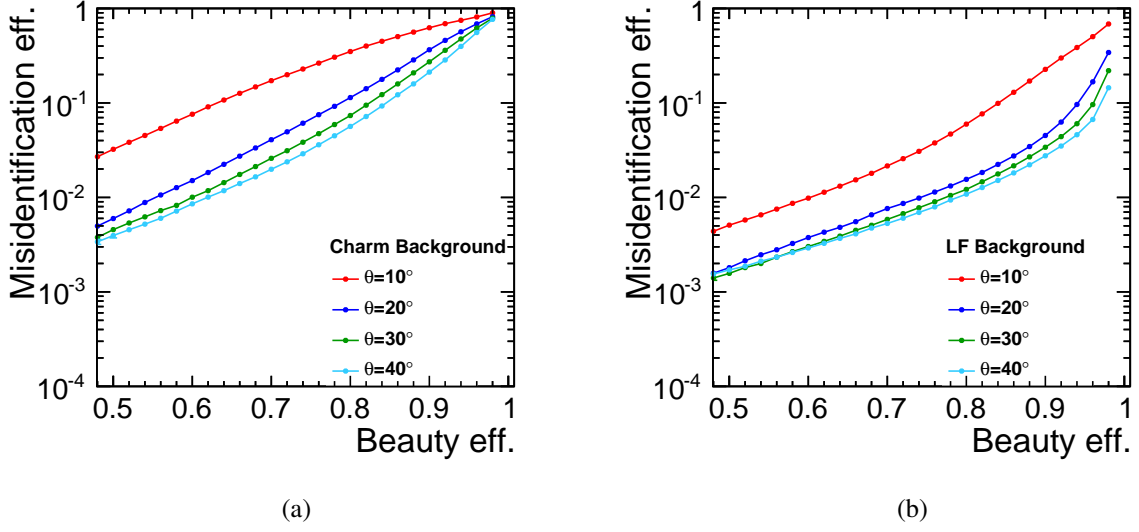


Figure 33: b-tag efficiency for jets dijet events at $\sqrt{s}=500$ GeV with different polar angles using the CDR geometry.

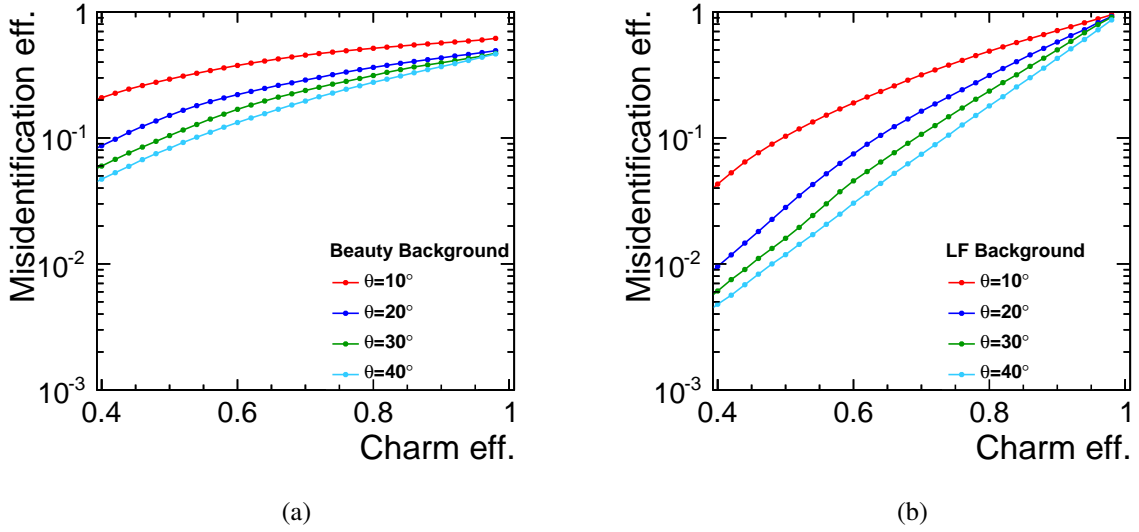


Figure 34: c-tag efficiency for jets in dijet events at $\sqrt{s}=500$ GeV with different polar angles using the CDR geometry.

A.3. Jets in dijet events at $\sqrt{s}=200$ GeV

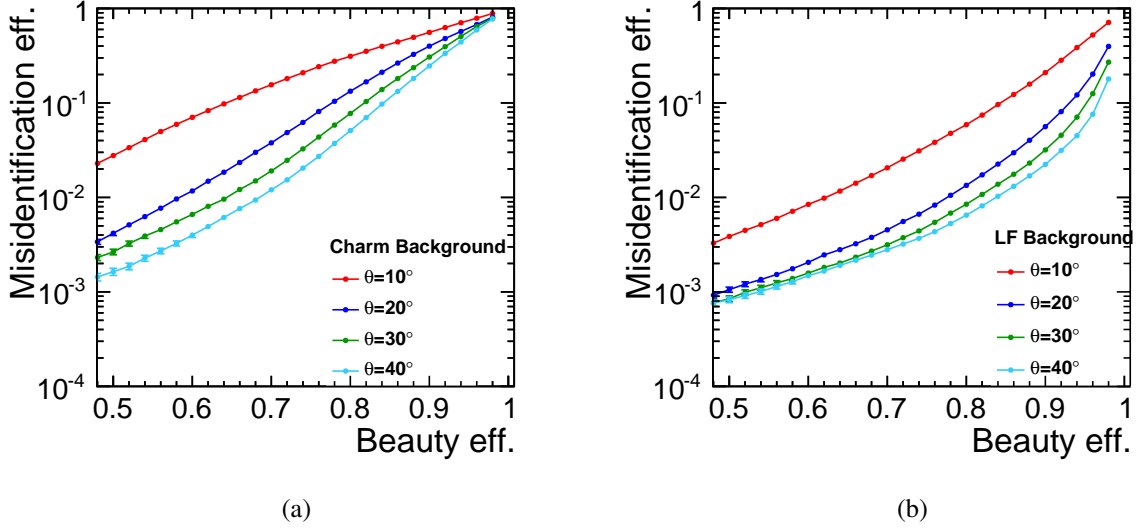


Figure 35: b-tag efficiency for jets dijet events at $\sqrt{s}=200$ GeV with different polar angles using the CDR geometry.

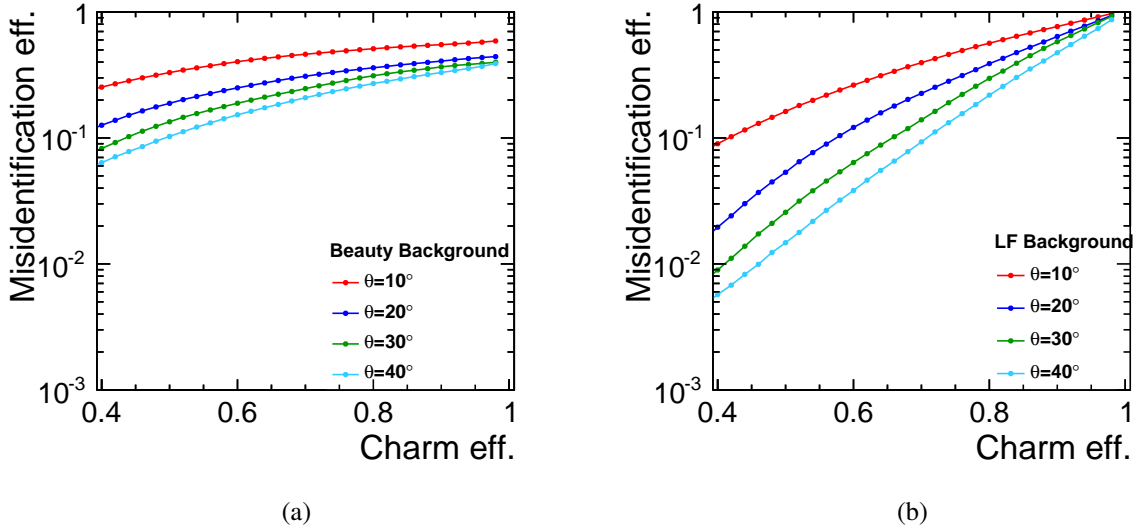


Figure 36: c-tag efficiency for jets in dijet events at $\sqrt{s}=200$ GeV with different polar angles using the CDR geometry.

A.4. Jets in dijet events at $\sqrt{s}=91$ GeV

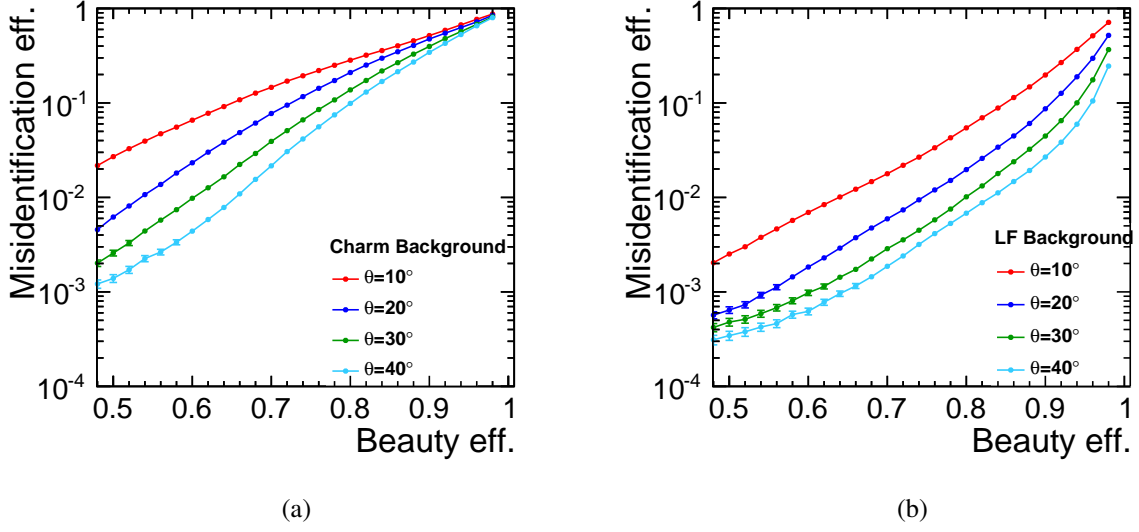


Figure 37: b-tag efficiency for jets dijet events at $\sqrt{s}=91$ GeV with different polar angles using the CDR geometry.

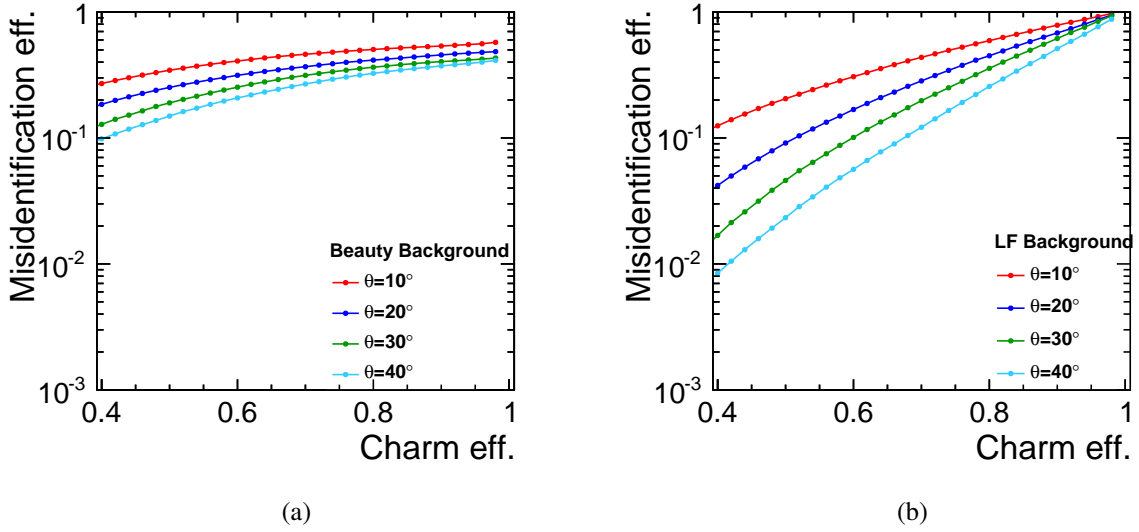


Figure 38: c-tag efficiency for jets in dijet events at $\sqrt{s}=91$ GeV with different polar angles using the CDR geometry.

B. Flavour tagging and jet-angle dependence for the *spirals* geometry

B.1. Jets in dijet events at $\sqrt{s}=1000$ GeV

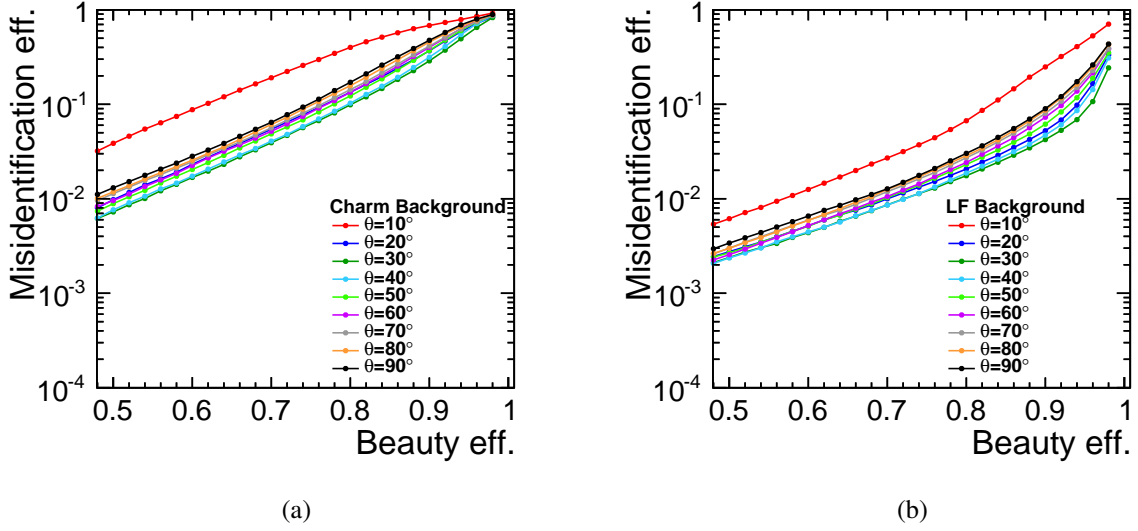


Figure 39: b-tag efficiency for jets in dijet events at $\sqrt{s}=1000$ GeV with different polar angles using the *spirals* geometry.

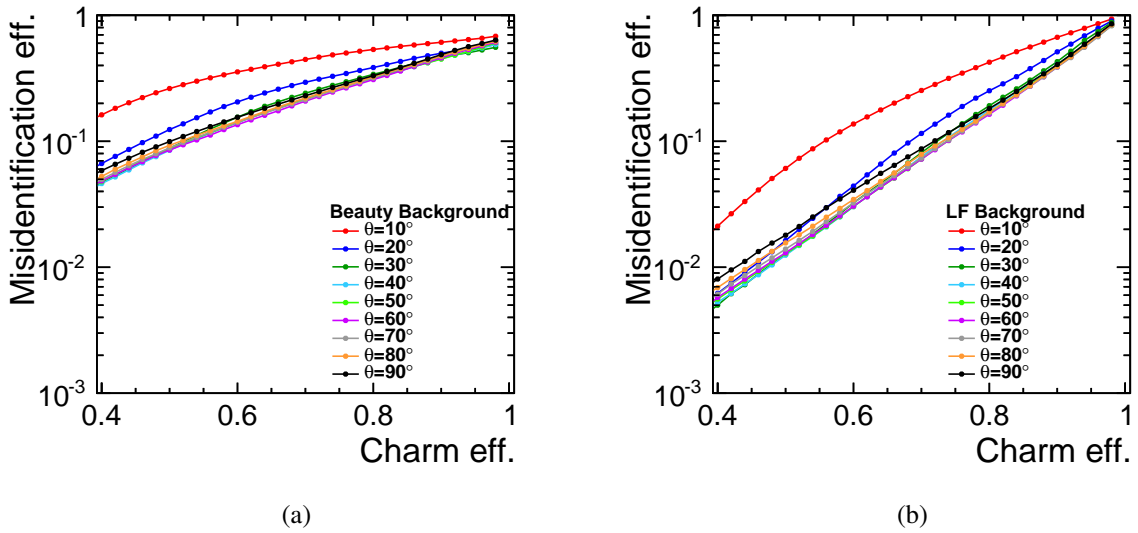


Figure 40: c-tag efficiency for jets in dijet events at $\sqrt{s}=1000$ GeV with different polar angles using the *spirals* geometry.

B.2. Jets in dijet events at $\sqrt{s}=500$ GeV

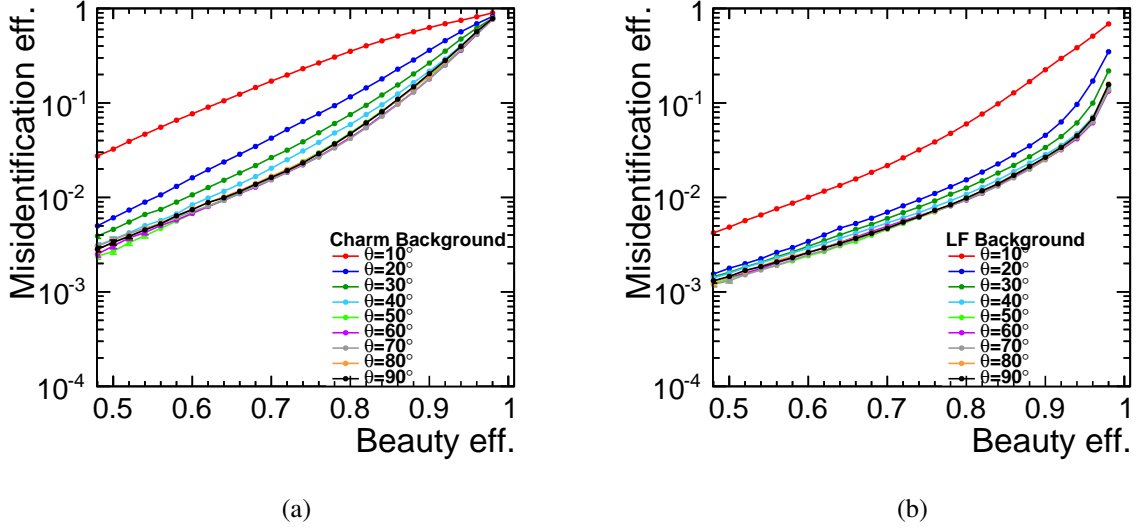


Figure 41: b-tag efficiency for jets in dijet events at $\sqrt{s}=500$ GeV with different polar angles using the *spirals* geometry.

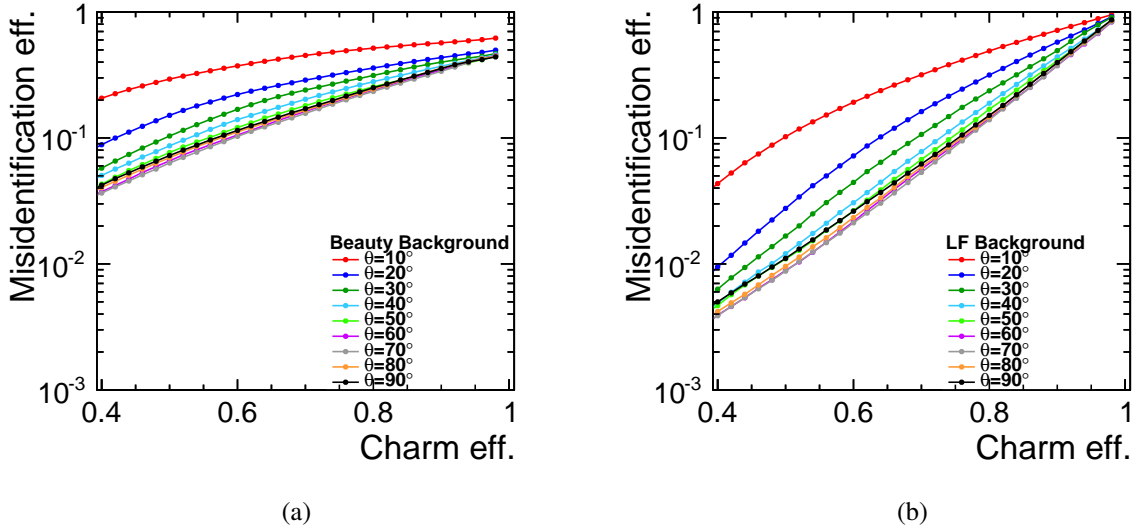
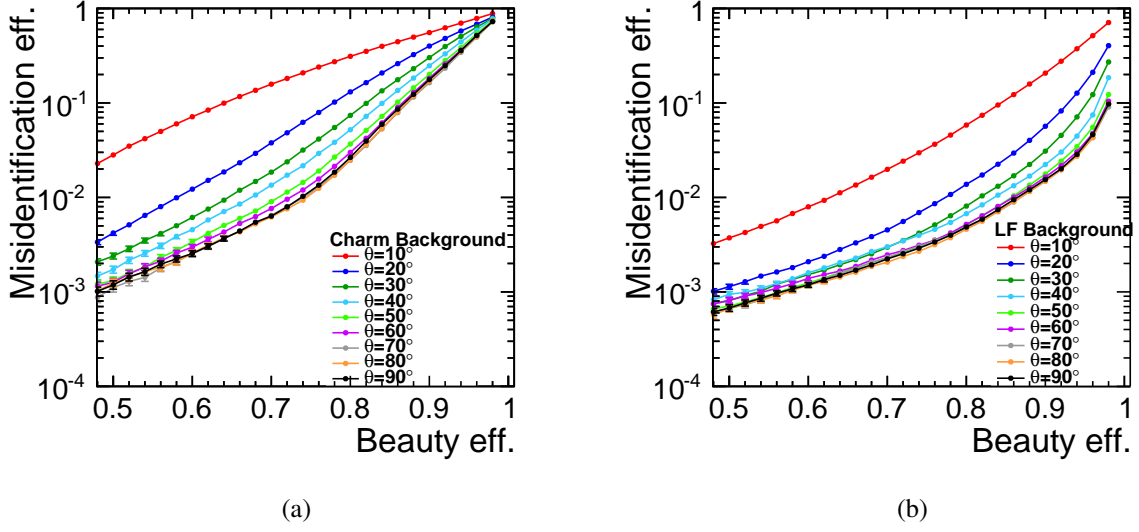
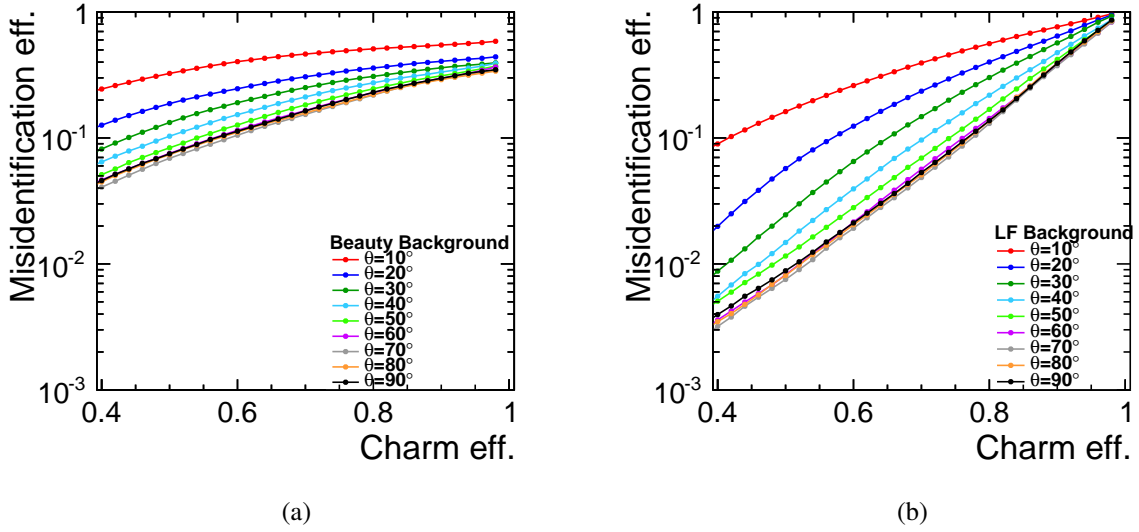
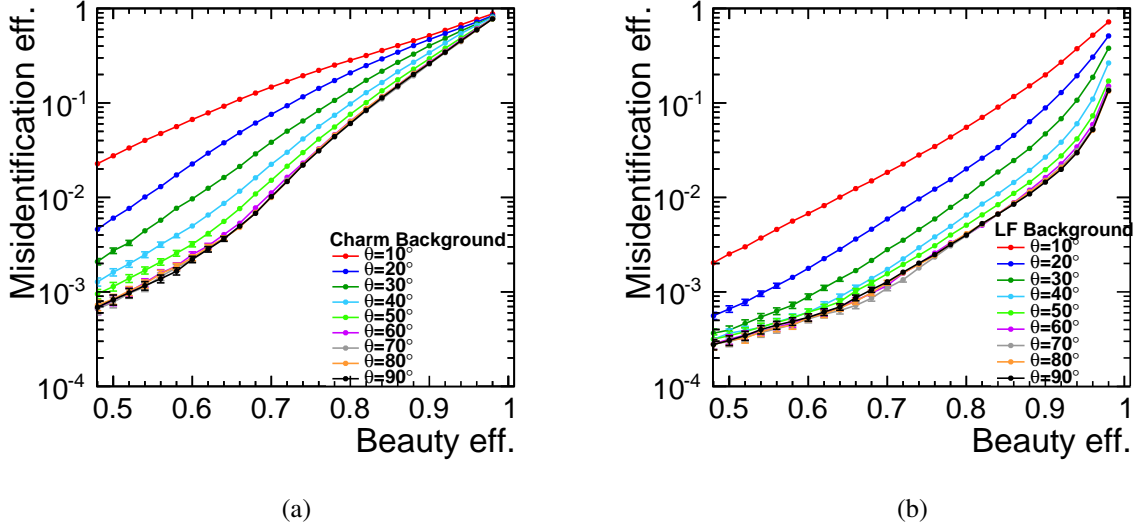
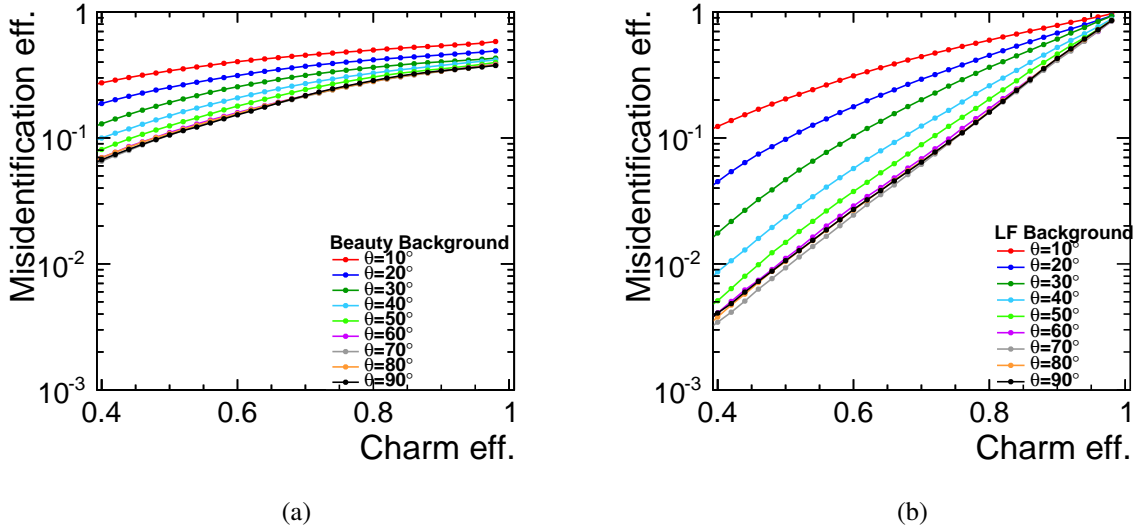


Figure 42: c-tag efficiency for jets in dijet events at $\sqrt{s}=500$ GeV with different polar angles using the *spirals* geometry.

B.3. Jets in dijet events at $\sqrt{s}=200$ GeV

 Figure 43: b-tag efficiency for jets in dijet events at $\sqrt{s}=200$ GeV with different polar angles using the *spirals* geometry.

 Figure 44: c-tag efficiency for jets in dijet events at $\sqrt{s}=200$ GeV with different polar angles using the *spirals* geometry.

B.4. Jets in dijet events at $\sqrt{s}=91$ GeV

 Figure 45: b-tag efficiency for jets in dijet events at $\sqrt{s}=91$ GeV with different polar angles using the *spirals* geometry.

 Figure 46: c-tag efficiency for jets in dijet events at $\sqrt{s}=91$ GeV with different polar angles using the *spirals* geometry.

C. Flavour tagging and jet-angle dependence for the *double_spirals* geometry

C.1. Jets in dijet events at $\sqrt{s}=1000$ GeV

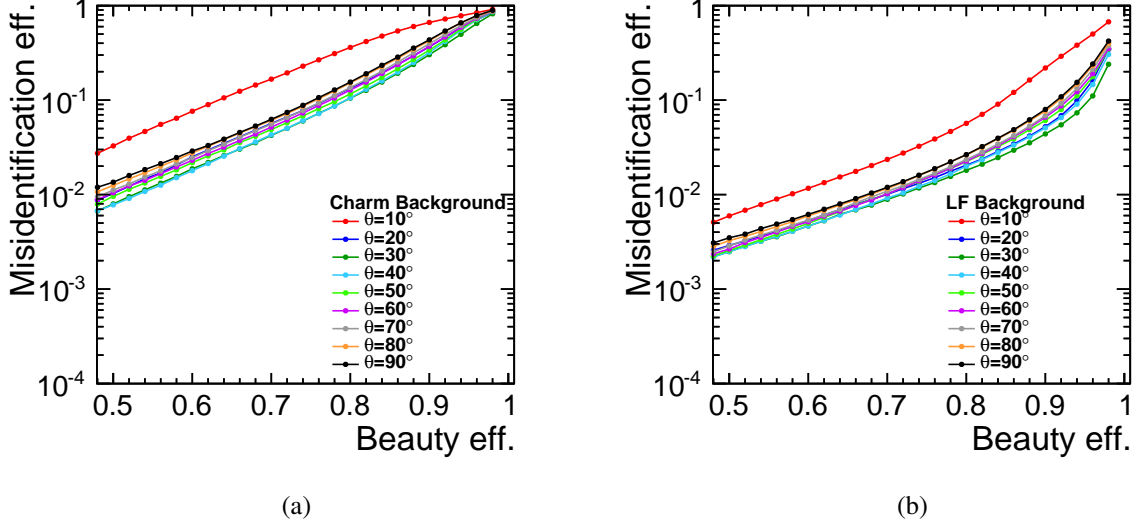


Figure 47: b-tag efficiency for jets in dijet events at $\sqrt{s}=1000$ GeV with different polar angles using the *double_spirals* geometry.

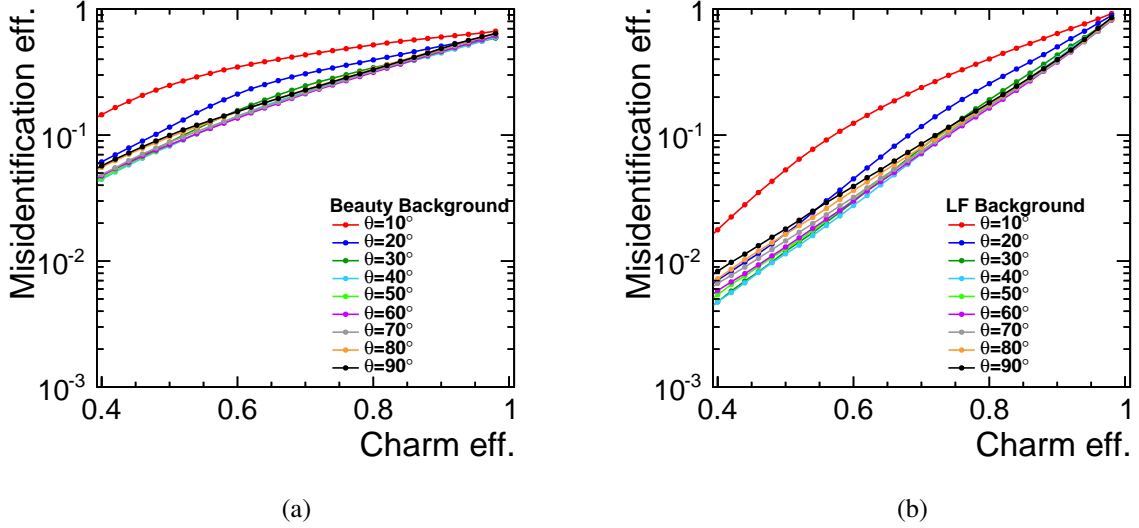


Figure 48: c-tag efficiency for jets in dijet events at $\sqrt{s}=1000$ GeV with different polar angles using the *double_spirals* geometry.

C.2. Jets in dijet events at $\sqrt{s}=500$ GeV

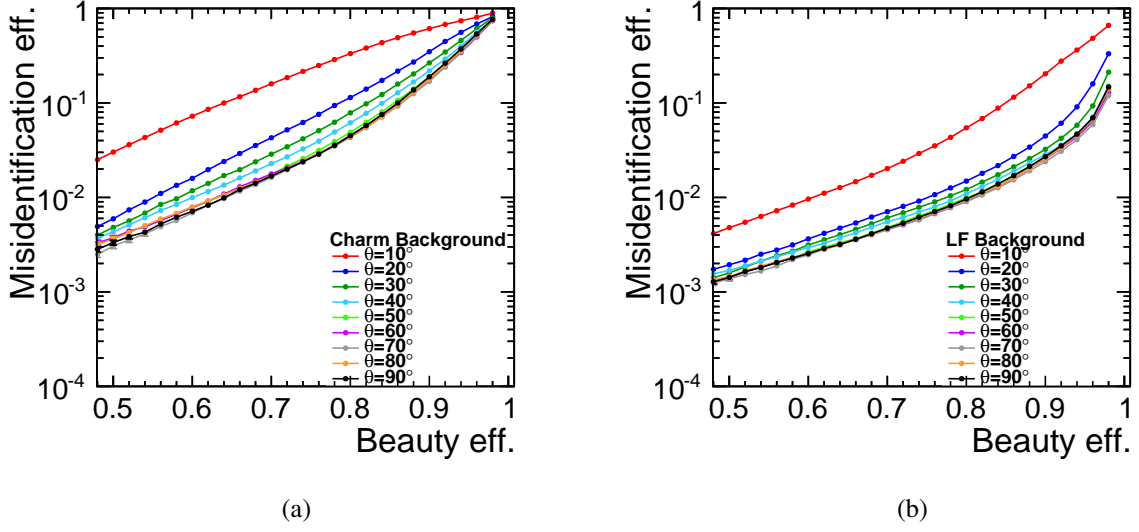


Figure 49: b-tag efficiency for jets in dijet events at $\sqrt{s}=500$ GeV with different polar angles using the *double_spirals* geometry.

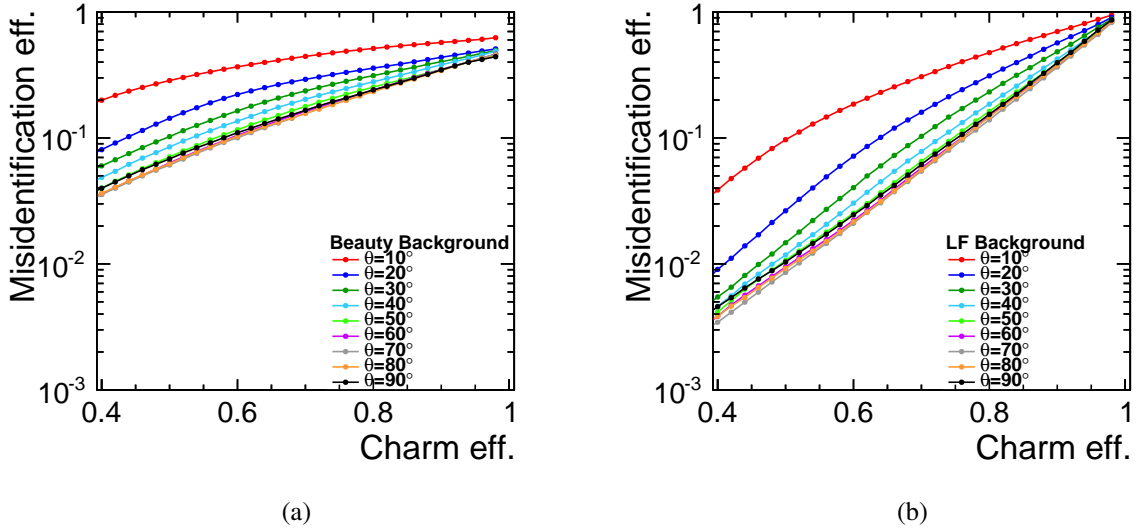


Figure 50: c-tag efficiency for jets in dijet events at $\sqrt{s}=500$ GeV with different polar angles using the *double_spirals* geometry.

C.3. Jets in dijet events at $\sqrt{s}=200$ GeV

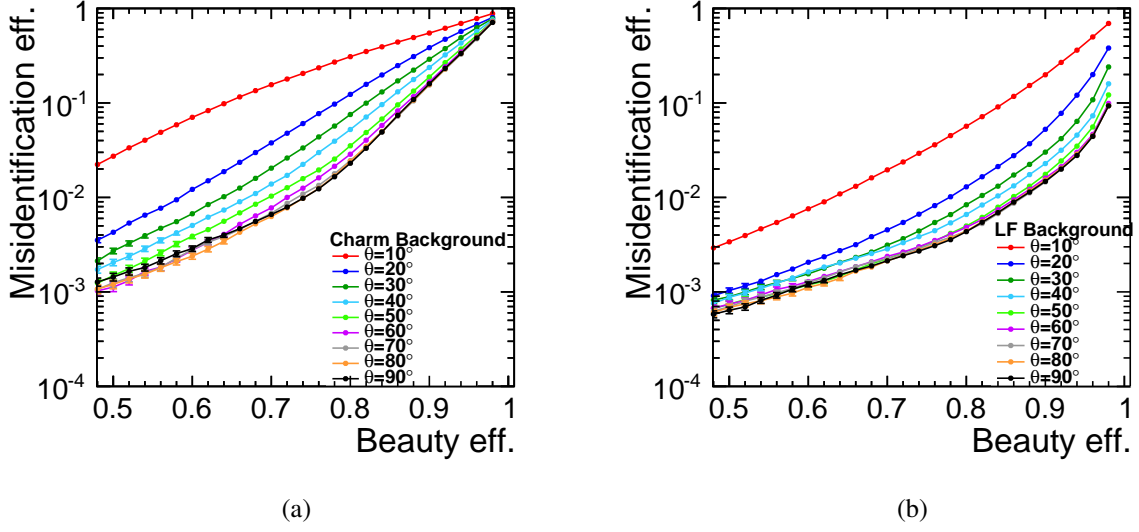


Figure 51: b-tag efficiency for jets in dijet events at $\sqrt{s}=200$ GeV with different polar angles using the *double_spirals* geometry.

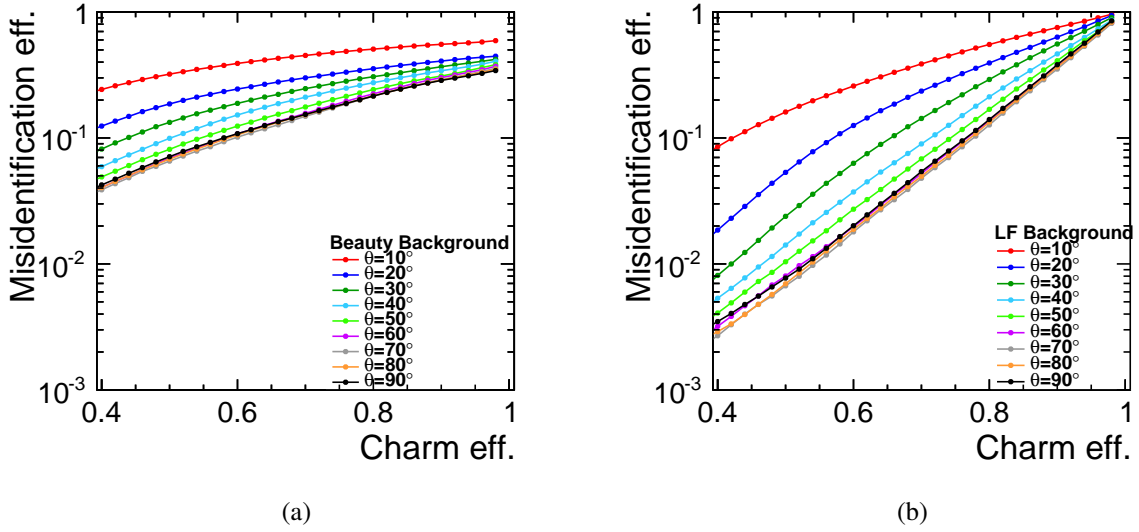


Figure 52: c-tag efficiency for jets in dijet events at $\sqrt{s}=200$ GeV with different polar angles using the *double_spirals* geometry.

C.4. Jets in dijet events at $\sqrt{s}=91$ GeV

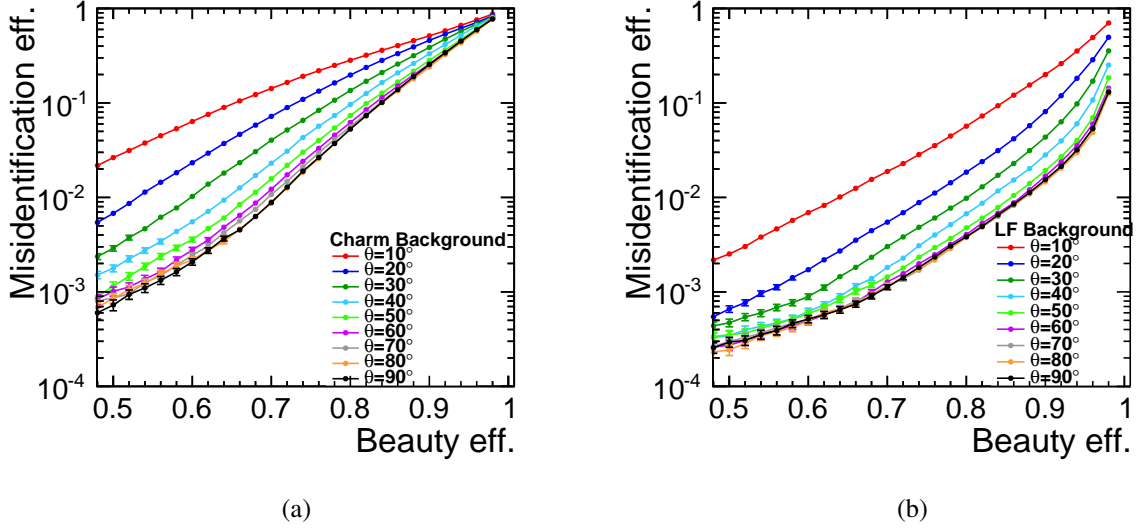


Figure 53: b-tag efficiency for jets in dijet events at $\sqrt{s}=91$ GeV with different polar angles using the *double_spirals* geometry.

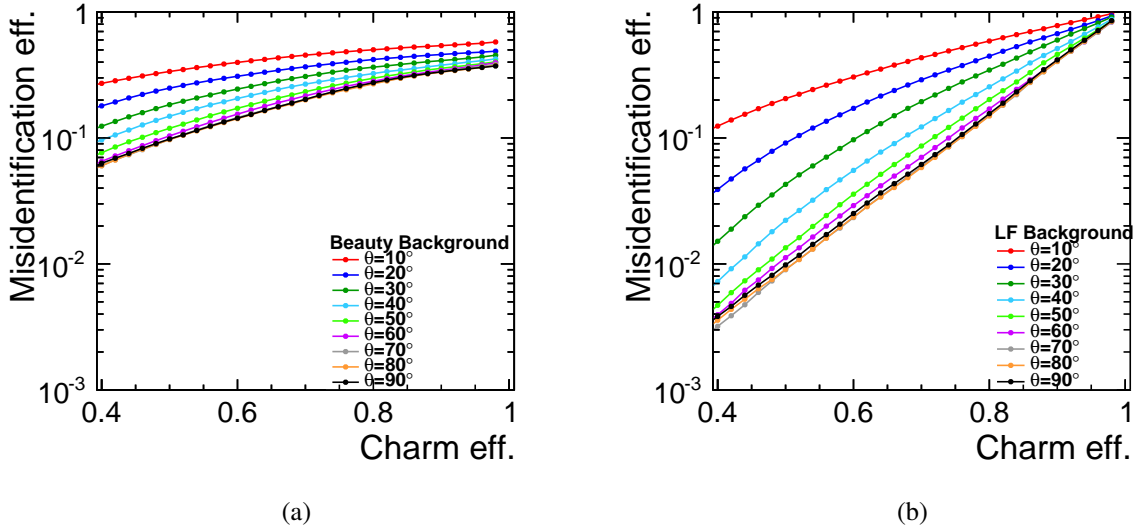


Figure 54: c-tag efficiency for jets in dijet events at $\sqrt{s}=91$ GeV with different polar angles using the *double_spirals* geometry.

D. spirals vs. CDR

D.1. Jets in dijet events at $\sqrt{s}=1000$ GeV

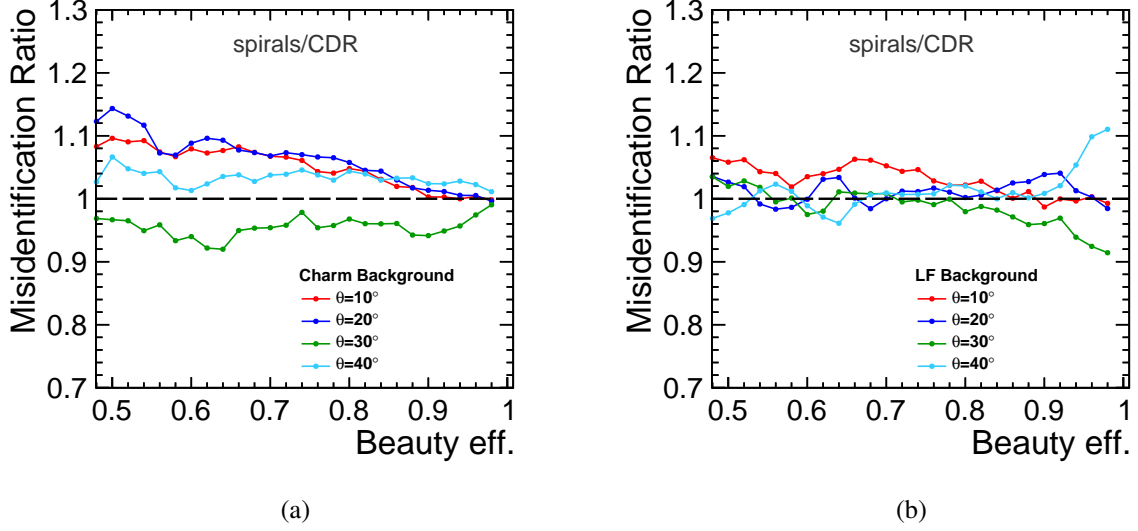


Figure 55: b-tagging: the ratio between the misidentification probabilities for the *spirals* and the CDR geometries based on jets in dijet events at $\sqrt{s}=1000$ GeV.

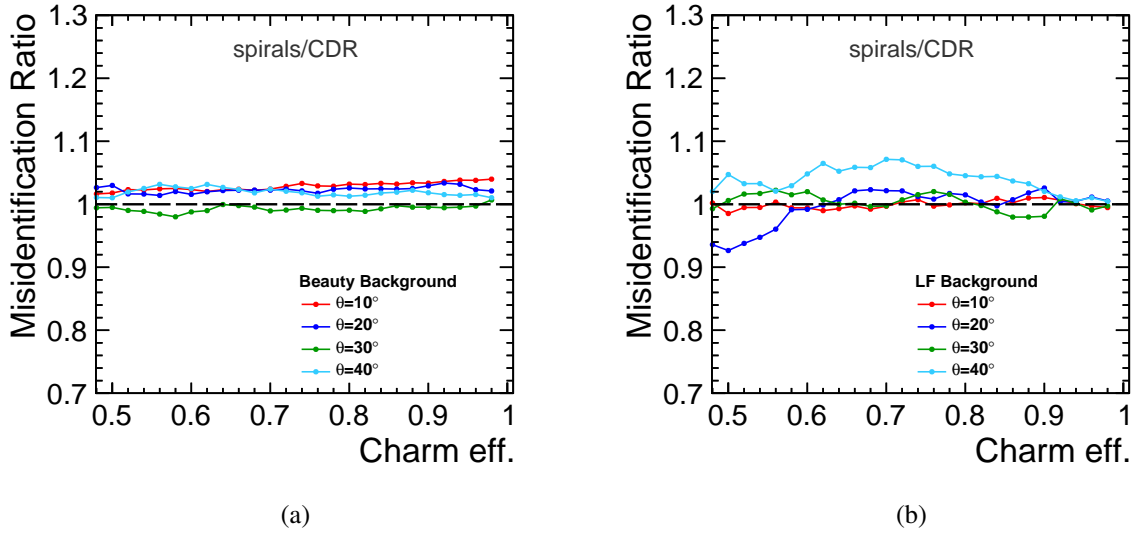


Figure 56: c-tagging: the ratio between the misidentification probabilities for the *spirals* and the CDR geometries based on jets in dijet events at $\sqrt{s}=1000$ GeV.

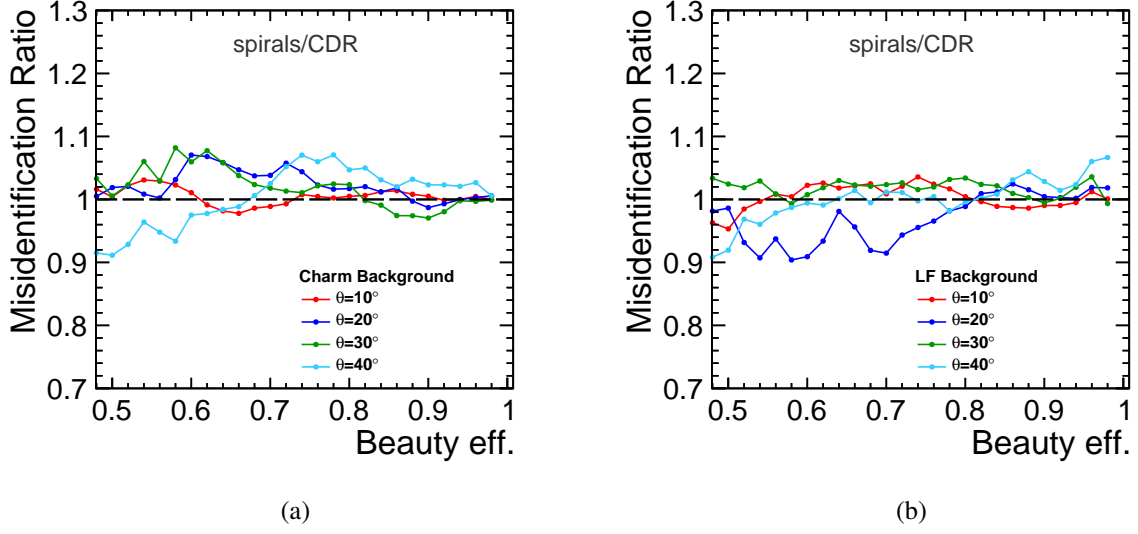
D.2. Jets in dijet events at $\sqrt{s}=500$ GeV

Figure 57: b-tagging: the ratio between the misidentification probabilities for the *spirals* and the CDR geometries based on jets in dijet events at $\sqrt{s}=500$ GeV.

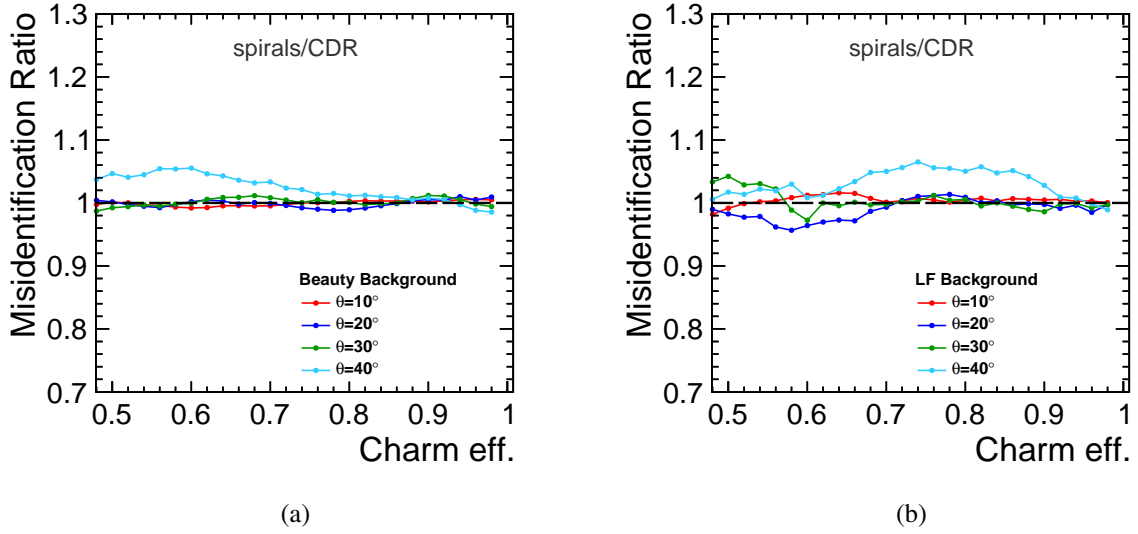


Figure 58: c-tagging: the ratio between the misidentification probabilities for the *spirals* and the CDR geometries based on jets in dijet events at $\sqrt{s}=500$ GeV.

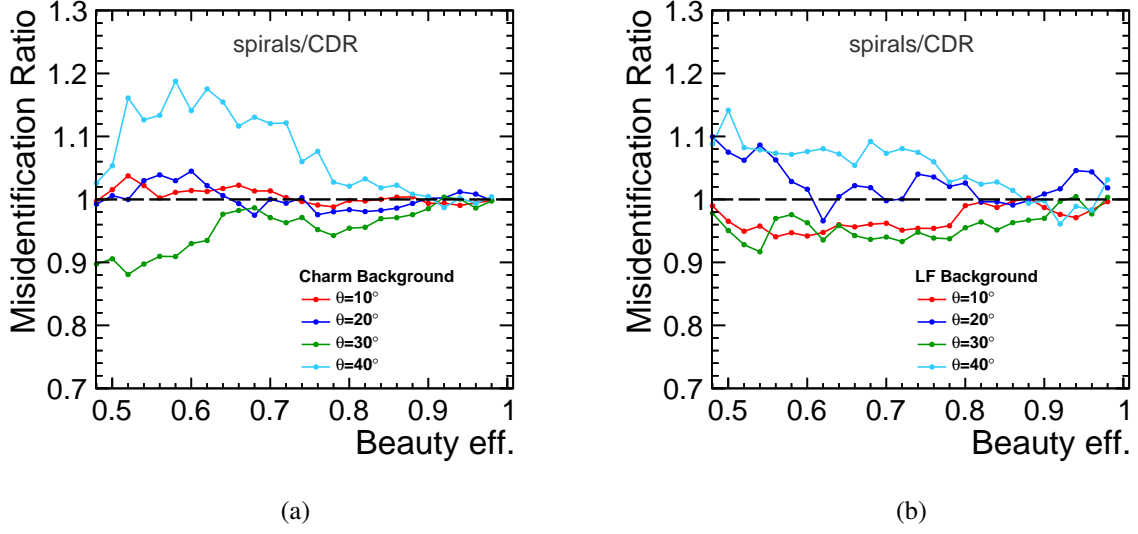
D.3. Jets in dijet events at $\sqrt{s}=200$ GeV

Figure 59: b-tagging: the ratio between the misidentification probabilities for the *spirals* and the CDR geometries based on jets in dijet events at $\sqrt{s}=200$ GeV.

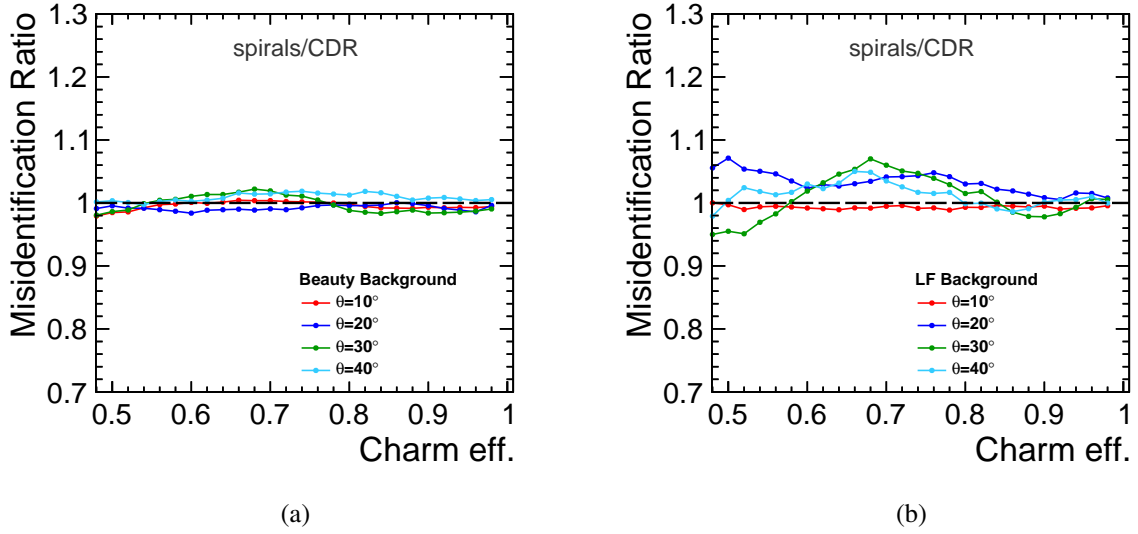


Figure 60: c-tagging: the ratio between the misidentification probabilities for the *spirals* and the CDR geometries based on jets in dijet events at $\sqrt{s}=200$ GeV.

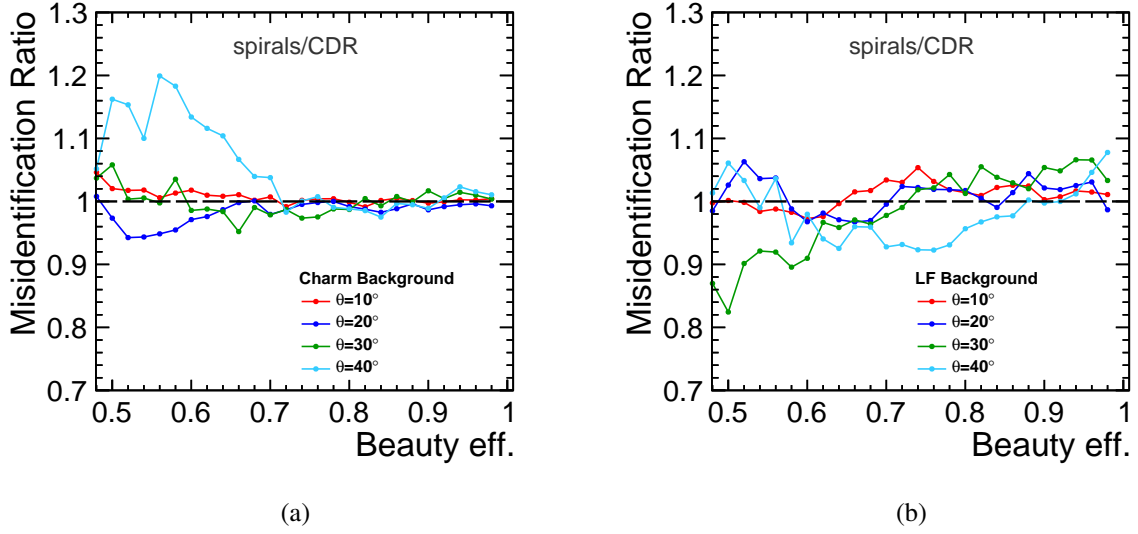
D.4. Jets in dijet events at $\sqrt{s}=91$ GeV

Figure 61: b-tagging: the ratio between the misidentification probabilities for the *spirals* and the CDR geometries based on jets in dijet events at $\sqrt{s}=91$ GeV.

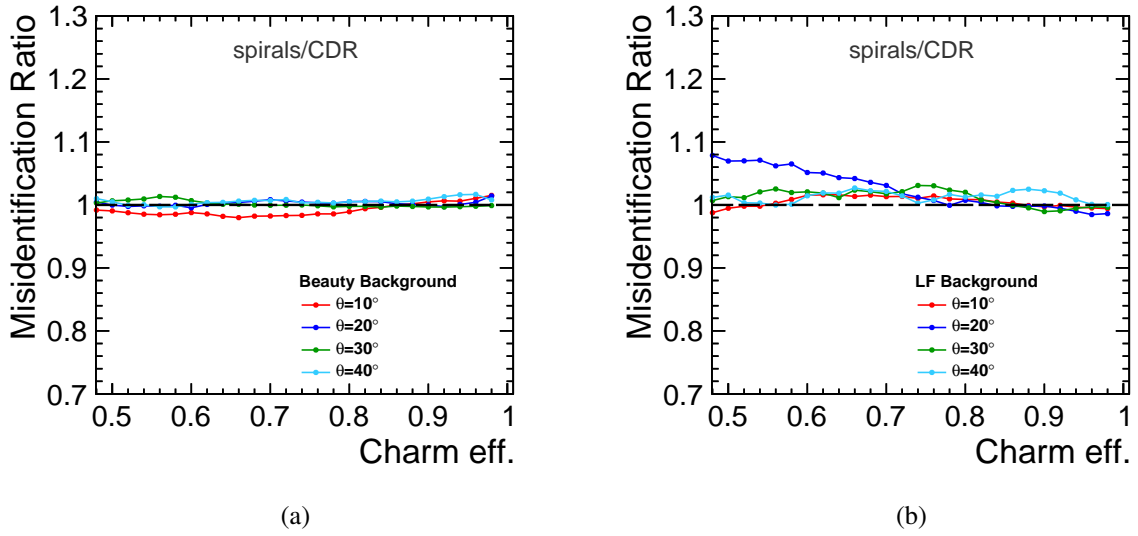


Figure 62: c-tagging: the ratio between the misidentification probabilities for the *spirals* and the CDR geometries based on jets in dijet events at $\sqrt{s}=91$ GeV.

E. *double_spirals* vs. CDR

E.1. Jets in dijet events at $\sqrt{s}=1000$ GeV

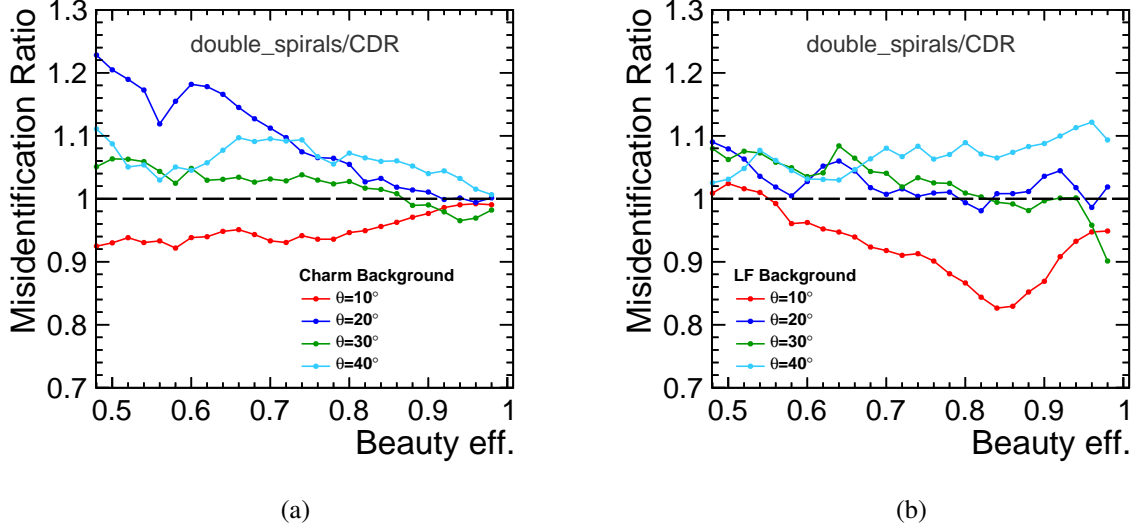


Figure 63: b-tagging: the ratio between the misidentification probabilities for the *double_spirals* and the CDR geometries based on jets in dijet events at $\sqrt{s}=1000$ GeV.

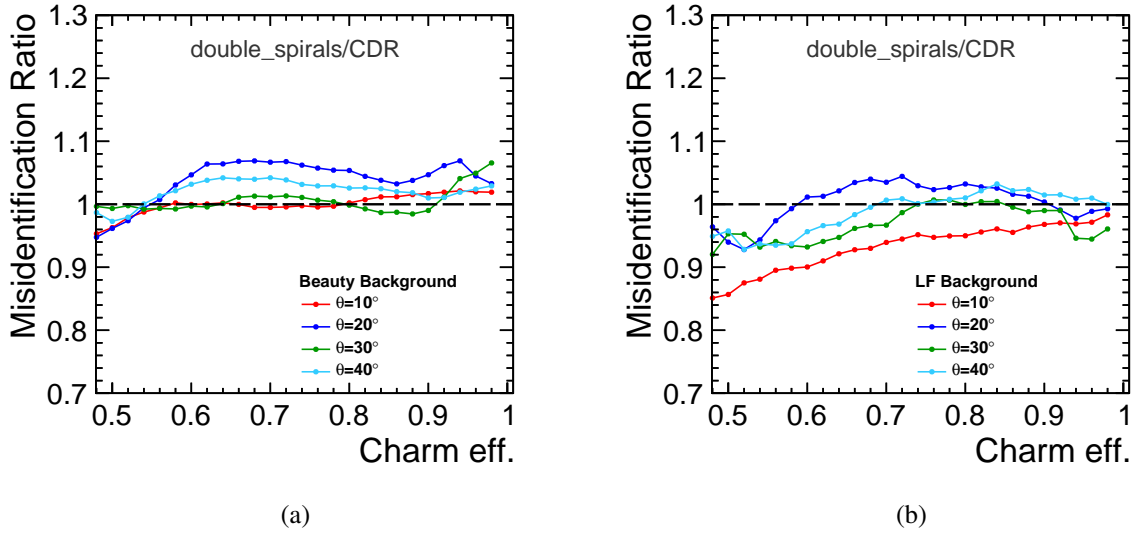


Figure 64: c-tagging: the ratio between the misidentification probabilities for the *double_spirals* and the CDR geometries based on jets in dijet events at $\sqrt{s}=1000$ GeV.

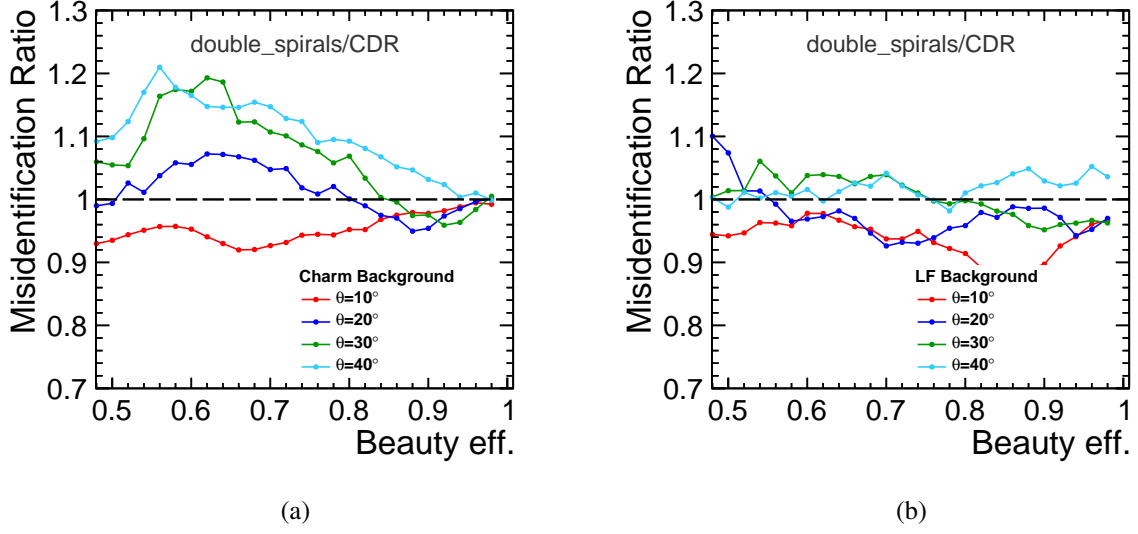
E.2. Jets in dijet events at $\sqrt{s}=500$ GeV

Figure 65: b-tagging: the ratio between the misidentification probabilities for the *double_spirals* and the CDR geometries based on jets in dijet events at $\sqrt{s}=500$ GeV.

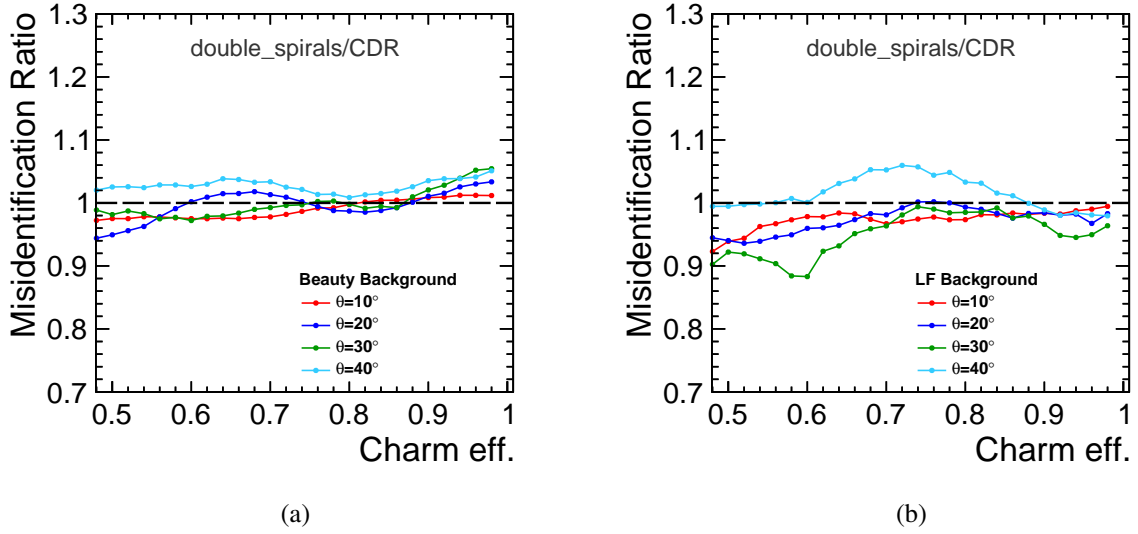


Figure 66: c-tagging: the ratio between the misidentification probabilities for the *double_spirals* and the CDR geometries based on jets in dijet events at $\sqrt{s}=500$ GeV.

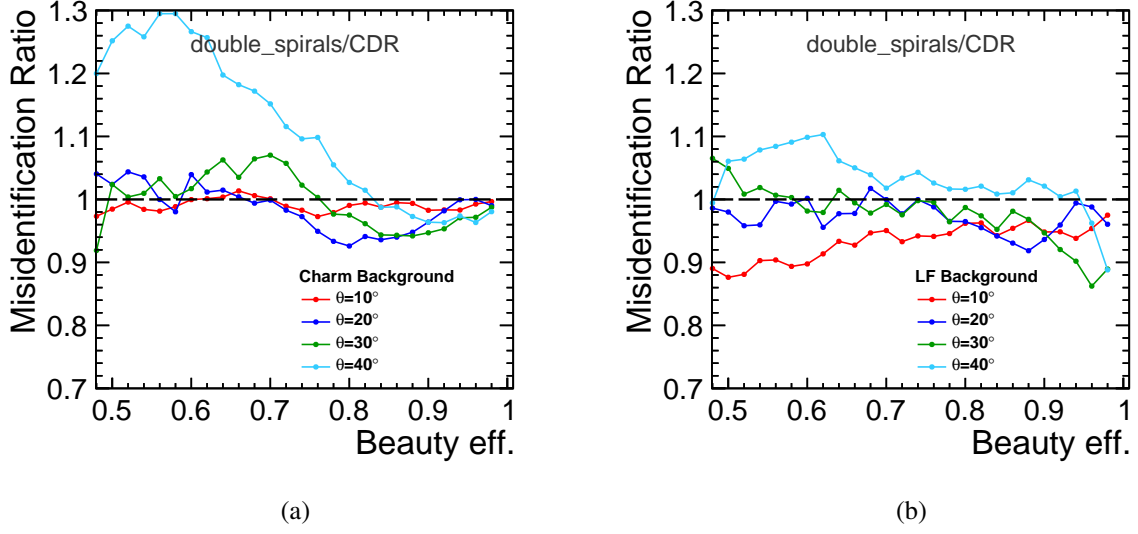
E.3. Jets in dijet events at $\sqrt{s}=200$ GeV

Figure 67: b-tagging: the ratio between the misidentification probabilities for the *double_spirals* and the CDR geometries based on jets in dijet events at $\sqrt{s}=200$ GeV.

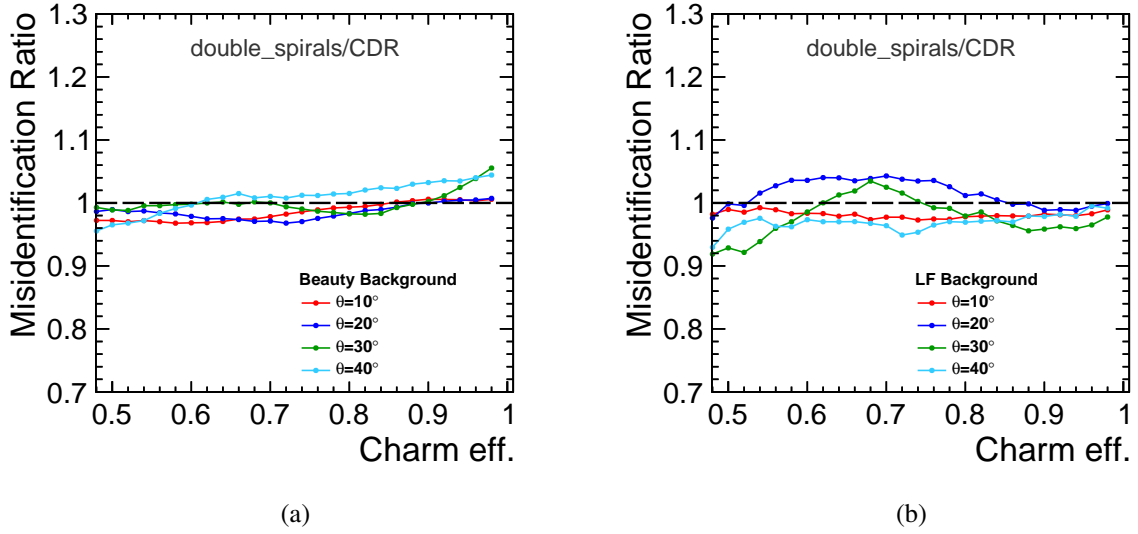


Figure 68: c-tagging: the ratio between the misidentification probabilities for the *double_spirals* and the CDR geometries based on jets in dijet events at $\sqrt{s}=200$ GeV.

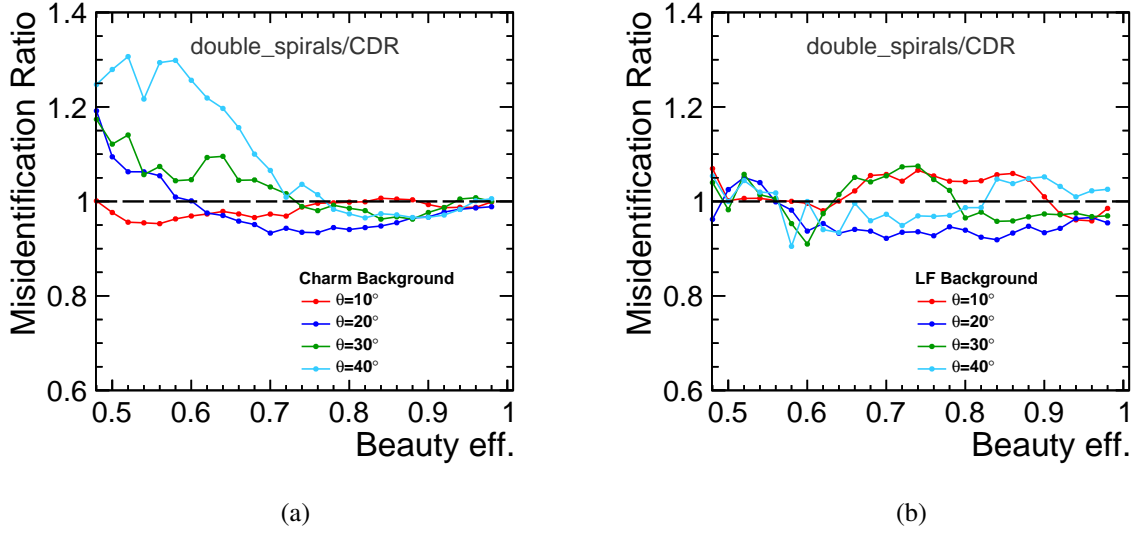
E.4. Jets in dijet events at $\sqrt{s}=91$ GeV

Figure 69: b-tagging: the ratio between the misidentification probabilities for the *double_spirals* and the CDR geometries based on jets in dijet events at $\sqrt{s}=91$ GeV.

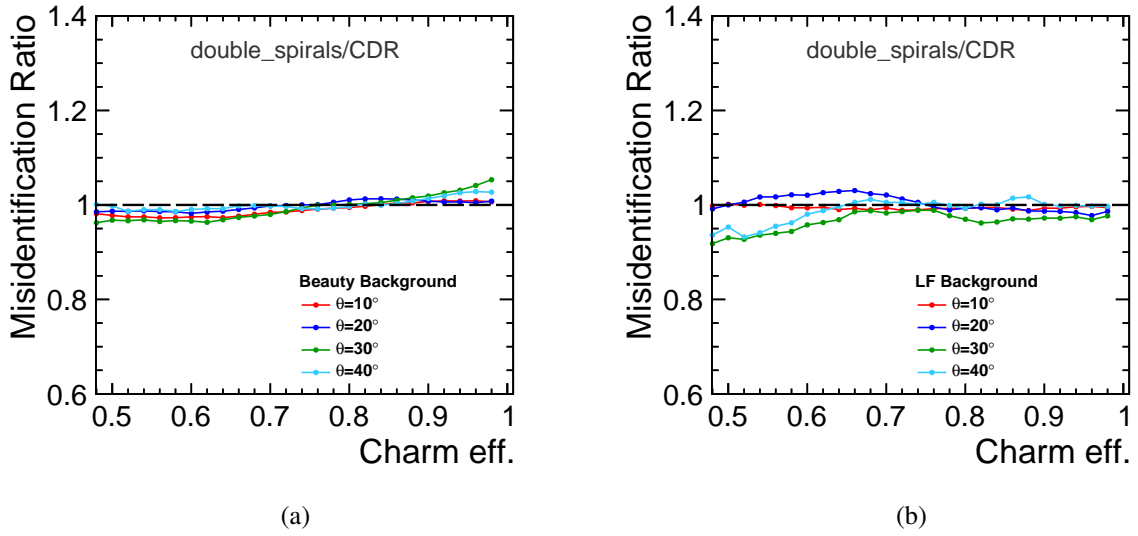


Figure 70: c-tagging: the ratio between the misidentification probabilities for the *double_spirals* and the CDR geometries based on jets in dijet events at $\sqrt{s}=91$ GeV.

F. *double_spirals* vs. *spirals*

F.1. Jets in dijet events at $\sqrt{s}=1000$ GeV

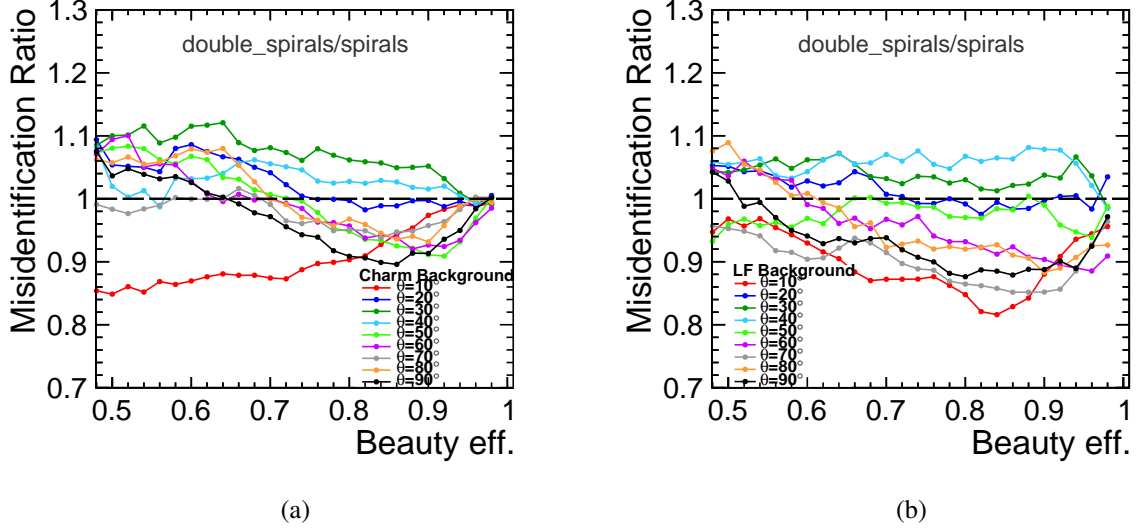


Figure 71: b-tagging: the ratio between the misidentification probabilities for the *double_spirals* and the *spirals* geometries based on jets in dijet events at $\sqrt{s}=1000$ GeV.

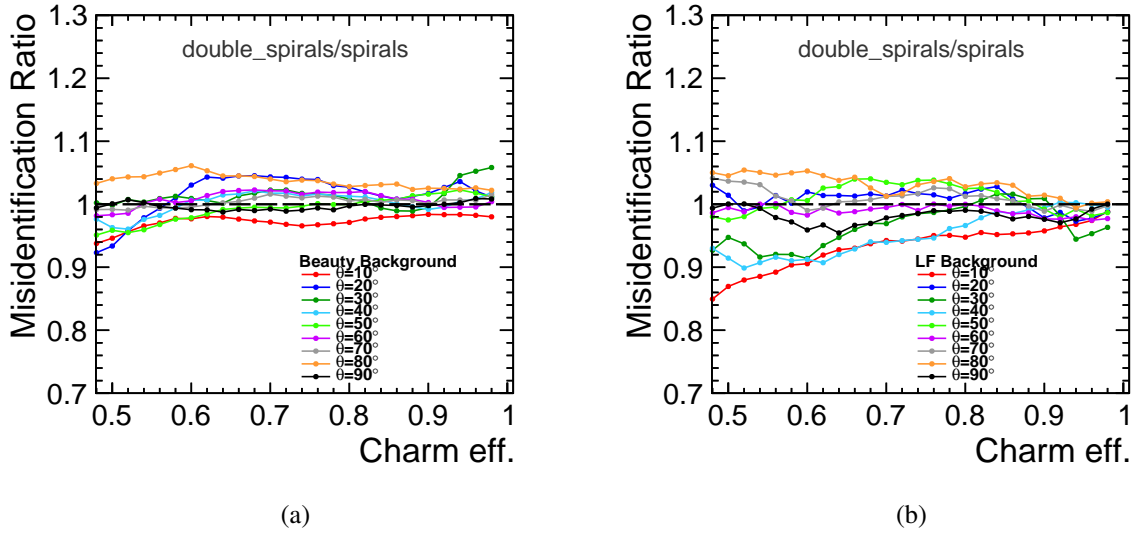


Figure 72: c-tagging: the ratio between the misidentification probabilities for the *double_spirals* and the *spirals* geometries based on jets in dijet events at $\sqrt{s}=1000$ GeV.

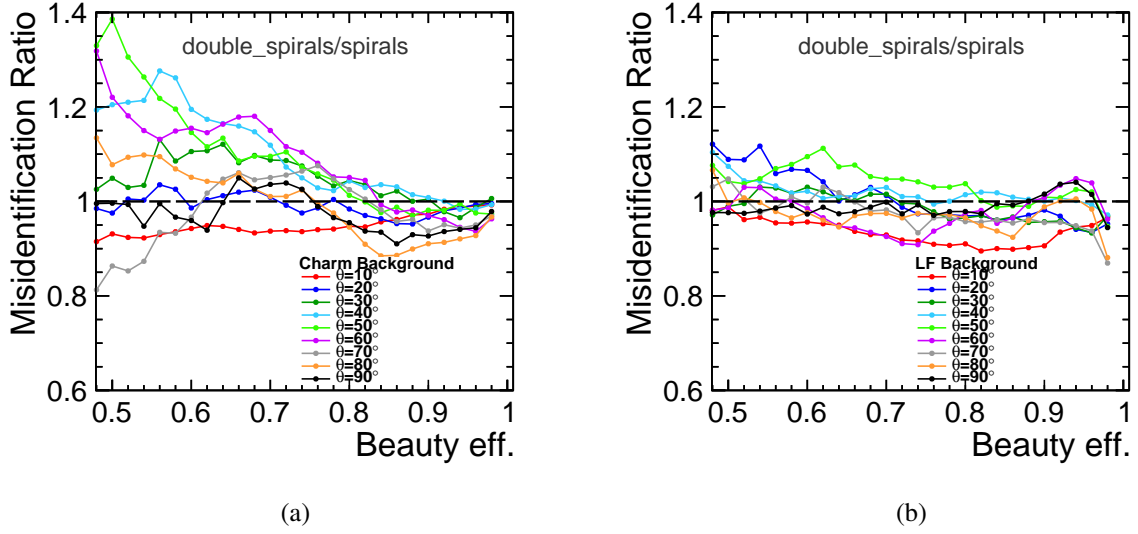
F.2. Jets in dijet events at $\sqrt{s}=500$ GeV

Figure 73: b-tagging: the ratio between the misidentification probabilities for the *double_spirals* and the *spirals* geometries based on jets in dijet events at $\sqrt{s}=500$ GeV.

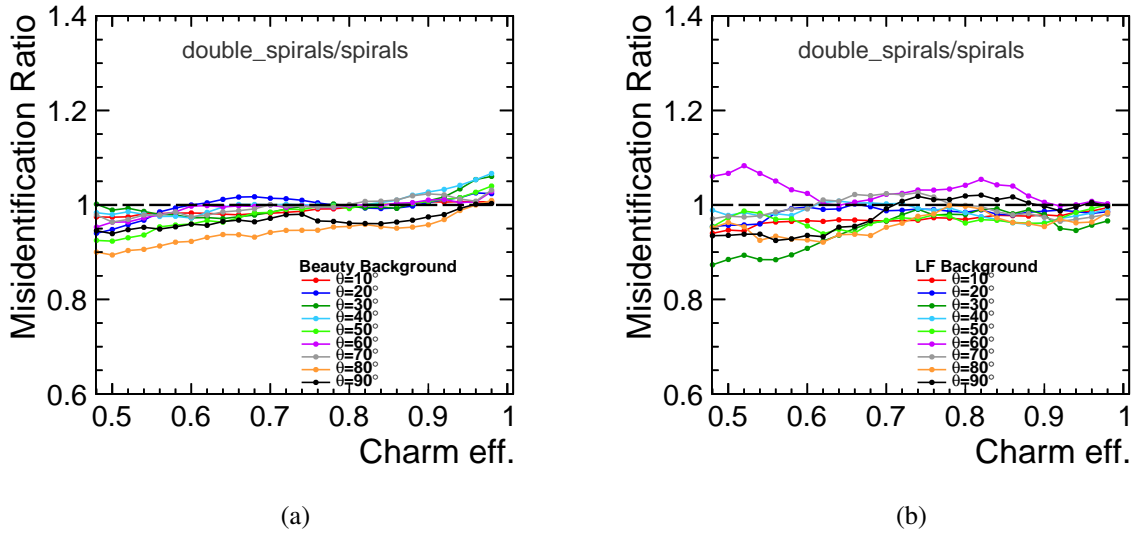


Figure 74: c-tagging: the ratio between the misidentification probabilities for the *double_spirals* and the *spirals* geometries based on jets in dijet events at $\sqrt{s}=500$ GeV.

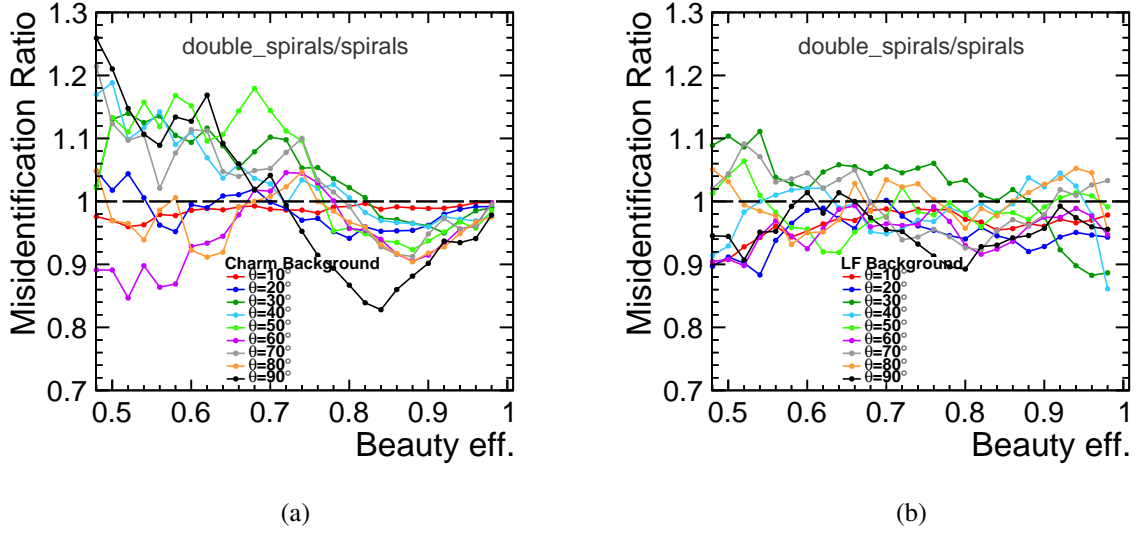
F.3. Jets in dijet events at $\sqrt{s}=200$ GeV

Figure 75: b-tagging: the ratio between the misidentification probabilities for the *double_spirals* and the *spirals* geometries based on jets in dijet events at $\sqrt{s}=200$ GeV.

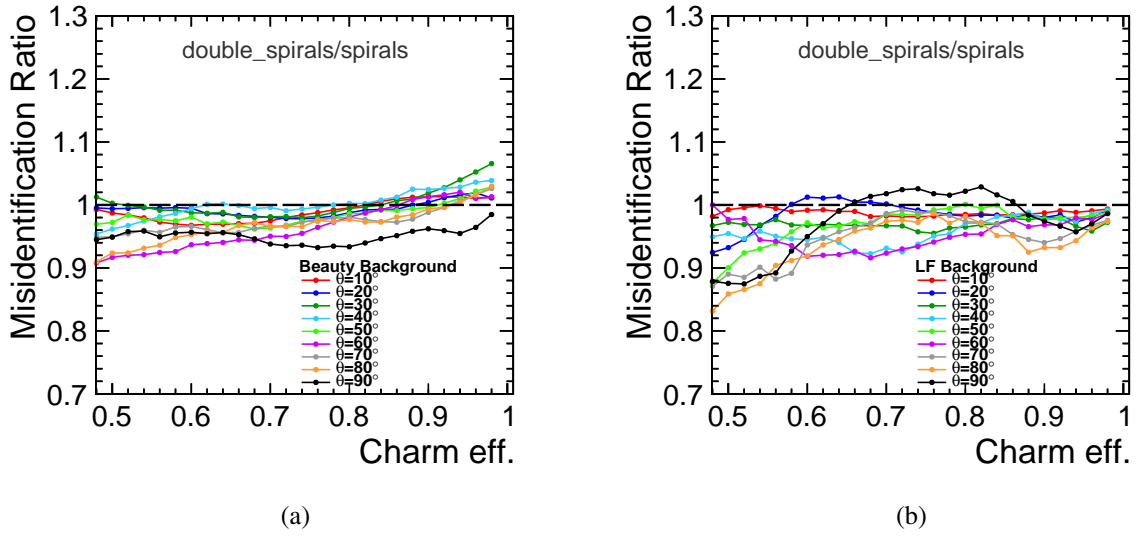


Figure 76: c-tagging: the ratio between the misidentification probabilities for the *double_spirals* and the *spirals* geometries based on jets in dijet events at $\sqrt{s}=200$ GeV.

F.4. Jets in dijet events at $\sqrt{s}=91$ GeV

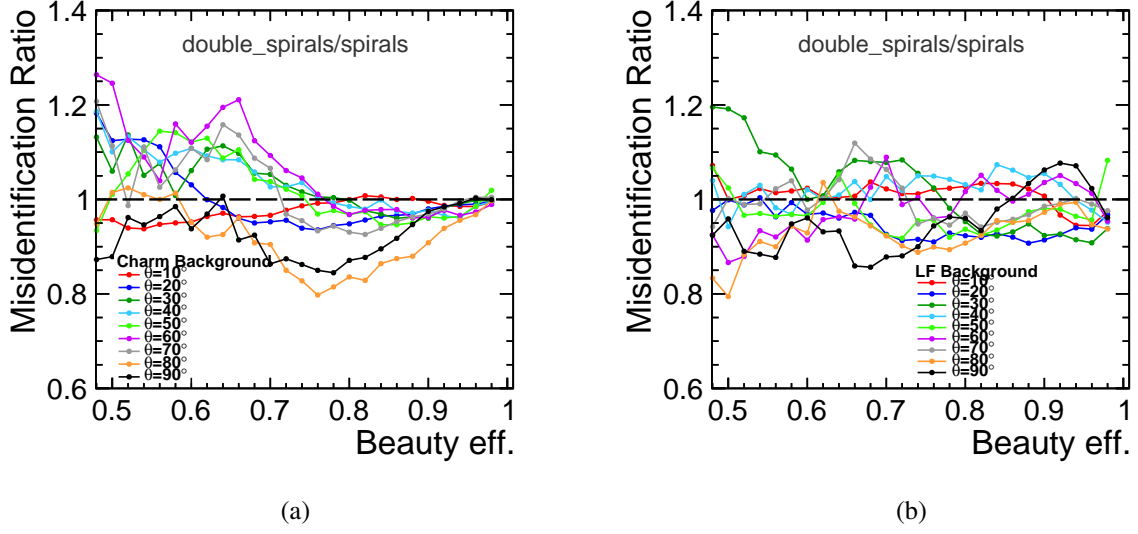


Figure 77: b-tagging: the ratio between the misidentification probabilities for the *double_spirals* and the *spirals* geometries based on jets in dijet events at $\sqrt{s}=91$ GeV.

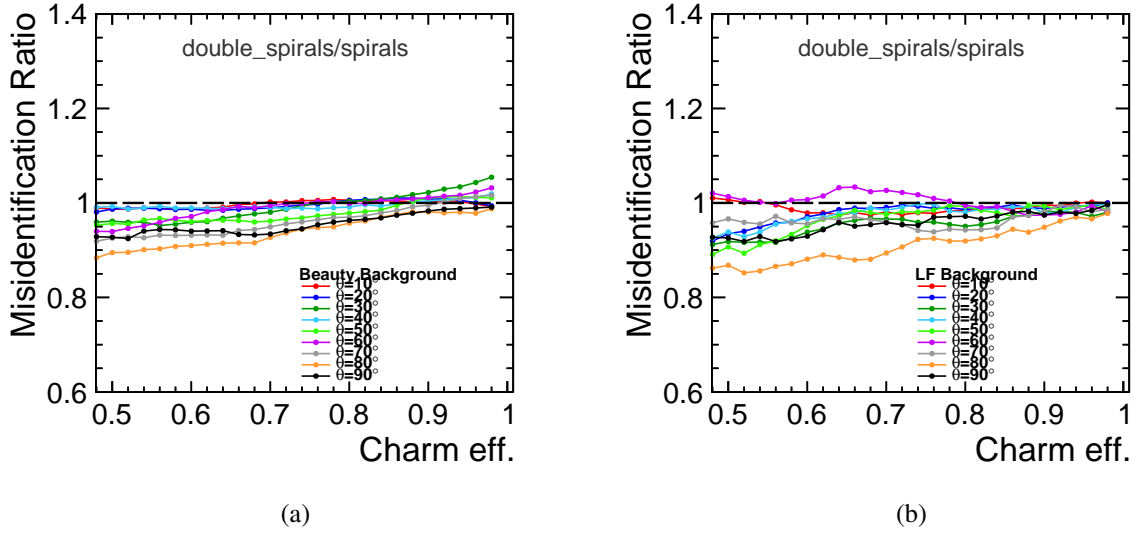


Figure 78: c-tagging: the ratio between the misidentification probabilities for the *double_spirals* and the *spirals* geometries based on jets in dijet events at $\sqrt{s}=91$ GeV.

References

- [1] L. Linssen et al., eds., *CLIC Conceptual Design Report: Physics and Detectors at CLIC*, CERN-2012-003, CERN, 2012, arXiv: [1202.5940](#) [[physics.ins-det](#)].
- [2] F. Duarte Ramos, H. Gerwig, M. Villarejo Bermudez, *CLIC inner detectors cooling simulations*, [LCD-Note-2013-007](#), CERN, 2013.
- [3] N. Alipour Tehrani, P. Roloff, P. Frossard, *Performance-Optimization Studies for the CLIC Vertex Detector*, [CERN-THESIS-2013-149](#), EPFL, Lausanne, 2013.
- [4] *GeomConverter*, URL: <http://lcsim.org/software/GeomConverter>.
- [5] N. Graf, J. McCormick, *Simulator for the linear collider (SLIC): A tool for ILC detector simulations*, AIP Conf. Proc. Vol. 867, Chicago, IL, 2006, p. 503.
- [6] S. Agostinelli et al., GEANT4 Collaboration, *GEANT4: A Simulation toolkit*, Nucl.Instrum.Meth. **A506** (2003) 250.
- [7] *Linear Collider Simulations (LCSim)*, URL: <http://lcsim.org/>.
- [8] M. Thomson, *Particle Flow Calorimetry and the PandoraPFA Algorithm*, Nucl.Instrum.Meth. **A611** (2009) 25, arXiv: [0907.3577](#) [[physics.ins-det](#)].
- [9] J. Marshall, A. Münnich, M. Thomson, *Performance of Particle Flow Calorimetry at CLIC*, Nucl.Instrum.Meth. **A700** (2013) 153, arXiv: [1209.4039](#) [[physics.ins-det](#)].
- [10] *LCFIPlus*, URL: <https://confluence.slac.stanford.edu/display/ilc/LCFIPlus>.
- [11] S. Catani et al., *New clustering algorithm for multi - jet cross-sections in $e^+ e^-$ annihilation*, Phys.Lett. **B269** (1991) 432.
- [12] C. Grefe et al., *ILCDIRAC, a DIRAC extension for the Linear Collider community*, 20th International Conference on Computing in High Energy and Nuclear Physics (CHEP 2013), vol. 513, CLICdp-Conf-2013-003, Amsterdam, the Netherlands, 2014, p. 032077.
- [13] C. Grefe, A. Münnich, *The CLIC_SiD_CDR Geometry for the CDR Monte Carlo Mass Production*, [LCD-Note-2011-009](#), CERN, 2011.
- [14] A. Münnich, A. Sailer, *The CLIC_ILD_CDR Geometry for the CDR Monte Carlo Mass Production*, [LCD-Note-2011-002](#), CERN, 2012.
- [15] G. Blanchot, D. Dannheim, C. Fuentes, *Power-pulsing schemes for vertex detectors at CLIC*, [CLICdp-Conf-2013-005](#), CERN, 2013.
- [16] T. Lastovicka, *Light Higgs Production and Decays to Pairs of Bottom and Charm Quarks at 3 TeV*, [LCD-Note-2011-036](#), CERN, 2012.